# A Map of Human Type 1 Diabetes Progression by Imaging Mass Cytometry

Damond, Nicolas ; Engler, Stefanie ; Zanotelli, Vito R T ; Schapiro, Denis ; Wasserfall, Clive H ; Kusmartseva, Irina ; Nick, Harry S ; Thorel, Fabrizio ; Herrera, Pedro L ; Atkinson, Mark A ; Bodenmiller, Bernd

Abstract: Type 1 diabetes (T1D) results from the autoimmune destruction of insulin-producing cells. A comprehensive picture of the changes during T1D development is lacking due to limited sample availability, inability to sample longitudinally, and the paucity of technologies enabling comprehensive tissue profiling. Here, we analyzed 1,581 islets from 12 human donors, including eight with T1D, using imaging mass cytometry (IMC). IMC enabled simultaneous measurement of 35 biomarkers with single-cell and spatial resolution. We performed pseudotime analysis of islets through T1D progression from snapshot data to reconstruct the evolution of cell loss and insulitis. Our analyses revealed that cell destruction is preceded by a cell marker loss and by recruitment of cytotoxic and helper T cells. The approaches described herein demonstrate the value of IMC for improving our understanding of T1D pathogenesis, and our data lay the foundation for hypothesis generation and follow-on experiments.

DOI: https://doi.org/10.1016/j.cmet.2018.11.014

# A Map of Human Type 1 Diabetes Progression by Imaging Mass Cytometry

**Nicolas Damond[1], Stefanie Engler[1], Vito R.T. Zanotelli[1,2], Denis Schapiro[1,6], Clive H. Wasserfall[3], Irina Kusmartseva[3], Harry S. Nick[4], Fabrizio Thorel[5], Pedro L. Herrera[5], Mark A. Atkinson[3], and Bernd Bodenmiller[1,7,*]**

[1]Institute of Molecular Life Sciences, University of Zurich, Zurich, Switzerland

[2]Systems Biology PhD Program, Life Science Zurich Graduate School, ETH Zurich and University of Zurich, Zurich, Switzerland

[3]Department of Pathology, Immunology, and Laboratory Medicine, College of Medicine, University of Florida, Gainesville, FL, USA

[4]Department of Neuroscience, College of Medicine, University of Florida, Gainesville, FL, USA

[5]Department of Genetic Medicine and Development, iGE3 and Centre facultaire du diabète, Faculty of Medicine, University of Geneva, Geneva, Switzerland

[6]Current addresses: Laboratory of Systems Pharmacology, Harvard Medical School, Boston, MA, USA and Broad Institute of MIT and Harvard, Cambridge, MA, USA.

[7]Lead contact

Correspondence: bernd.bodenmiller@imls.uzh.ch

## SUMMARY

Type 1 diabetes (T1D) results from the autoimmune destruction of insulin-producing β cells. A comprehensive picture of the changes during T1D development is lacking due to limited sample availability, inability to sample longitudinally, and the paucity of technologies enabling comprehensive tissue profiling. Here, we analyzed 1,581 islets from 12 human donors, including eight with T1D, using imaging mass cytometry (IMC). IMC enabled simultaneous measurement of 35 biomarkers with single-cell and spatial resolution. We performed pseudotime analysis of islets through T1D progression from snapshot data to reconstruct the evolution of β cell loss and insulitis. Our analyses revealed that β cell destruction is preceded by a β cell marker loss and by recruitment of cytotoxic and helper T cells. The approaches described herein demonstrate the value of IMC for improving our understanding of T1D pathogenesis, and our data lay the foundation for hypothesis generation and follow-on experiments.

## INTRODUCTION

Type 1 diabetes (T1D) is a chronic condition thought to result from an autoimmune attack on insulin-producing β cells in the pancreatic islets of Langerhans (Atkinson et al., 2014). The disorder, characterized by overt hyperglycemia, develops from a poorly understood combination of genetic and environmental factors and is thought to involve complex interactions between islets and cells of the immune system (Boldison and Wong, 2016). The study of human T1D has been limited by sample availability. Further, imaging of the pancreatic islets cannot be performed *in vivo*, and pancreatic biopsies, which would enable longitudinal studies of the changes of islet cell composition and cell-cell interactions, are not undertaken due to the associated investigational risks. Consequently, much of our knowledge regarding T1D pancreas pathology is derived from mouse models and limited analysis of individual specimens obtained from autopsy collections of human pancreata (Gepts, 1965; Foulis and Stewart, 1984). To enable more systematic studies of human pancreatic T1D tissue, biobanks such as the Network for Pancreatic Organ donors with Diabetes (nPOD) or the Human Pancreas Analysis Program (HPAP) (Campbell-Thompson et al., 2012a; Marchetti et al., 2018) have been established to collect tissues from organ donors.

In recent years, studies of human pancreas samples from these biobanks have provided valuable information regarding the pathogenesis and natural history of this disease. For example these analyses revealed the presence of islet-specific autoreactive $CD8^+$ T cells in the pancreata of donors with T1D (Coppieters et al., 2012). It has also become evident that insulitis is less aggressive amongst T1D patients than it is in mouse models of T1D (Meier et al., 2005; Coppieters et al., 2012). Heterogeneity is observed on the cellular level, as the loss of functional β cell mass is not only caused by β cell destruction but also by dysfunctional β cells (Chen et al., 2017). On the individual pancreas level, insulitis often occurs in a lobular fashion and even islets in proximity show the presence and absence of insulitis (Gianani et al., 2010; Rodriguez-Calvo et al., 2015). A large degree of inter-patient heterogeneity is observed in terms of insulitis frequency

and composition, residual β cell mass, and pace of β cell destruction (Campbell-Thompson et al., 2016), with insulitic lesions sometimes persisting for decades after diagnosis (Meier et al., 2005; Coppieters et al., 2012).

Despite these findings, our understanding of T1D progression in human patients is limited. An understanding of how cell types, cell states, and cell-cell interactions evolve during T1D development is essential to designing strategies to cure or halt this disorder. The lack of a comprehensive spatially resolved cellular analysis of the T1D lesion is due, at least in part, to the fact that only recently have highly multiplexed tissue imaging technologies emerged that allow for comprehensive studies of tissue from rare donor samples. These approaches include imaging techniques that are based on cyclic immunofluorescence (Schubert et al., 2006; Gerdes et al., 2013; Zrazhevskiy and Gao, 2013; Lin et al., 2015; Goltsev et al., 2018; Gut et al., 2018), epitope-targeted mass spectrometry (Angelo et al., 2014; Giesen et al., 2014), and RNA detection (Ke et al., 2013; Lee et al., 2014; Chen et al., 2015; Schulz et al., 2018). These methods provide a comprehensive view of marker distribution and tissue composition and are, therefore, poised to unlock some of the mysteries surrounding the pathogenesis of T1D and other complex disorders (Bodenmiller, 2016).

Here we used imaging mass cytometry (IMC) to analyze pancreas tissue from four control organ donors as well as four at onset and four with long-term T1D. IMC combines laser ablation with mass cytometry to enable simultaneous evaluation of up to 50 biomarkers from tissue sections stained with metal-tagged antibodies (Giesen et al., 2014). Using IMC data, we generated a map of islet heterogeneity as well as interactions between islet and immune cells. Pseudotime analysis at the islet-level enabled us to reconstruct islet evolution through T1D progression from the snapshot data from the 12 donors. These analyses revealed that a large fraction of islets from patients with recent-onset T1D retain a near-normal fraction of β cells but that the phenotype of these β cells is altered prior to β cell destruction. Finally, we investigated the dynamics of islet-associated immune cells and the evolution of cell-cell interactions during

T1D progression. We observed that, although association between islet cells and immune cells is rare, both cytotoxic and helper T cells are simultaneously recruited to β cell-rich islets during T1D onset, indicating the assembly of a destructive immune motif.

# RESULTS

## Preprocessing of Human T1D Samples and Image Acquisition

In IMC, tissue sections are labeled with metal-conjugated antibodies (Figure 1A). During image acquisition, a laser ablates the tissue spot-by-spot at a resolution of 1 µm, and the clouds of tissue particles are analyzed by mass cytometry. The metal composition of the ablated tissue and thus, by inference, the antibody and epitope content is used to create images pixel-by-pixel, each pixel corresponding to one laser shot (Giesen et al., 2014). To enable IMC measurement of pancreas specimens from human donors with T1D, we designed a novel panel of 35 metal-tagged antibodies targeting key islet cell antigens as well as immune cell markers (Table 1 and STAR methods).

We selected 12 cases from the nPOD biorepository to represent recent-onset T1D (< 0.5 years, $N = 4$), long-standing T1D duration (≥ 8 years, $N = 4$), and controls without diabetes ($N = 4$) and for each donor analyzed two sections originating from different anatomical regions of the pancreas (tail, body, or head) (Table S1). Because the speed of data acquisition prevents imaging of entire pancreas sections, we used immunofluorescence (IF) to perform a pre-selection of areas of interest (Figure S1A and STAR Methods). We then stained the same sections with metal-labeled primary antibodies (Table 1) and imaged the selected areas by IMC. Our measurements yielded 845 multiplexed images that included 1581 islets (each with ≥ 10 cells); data were obtained in 37 channels corresponding to the 35 antibodies and two DNA counterstains in our panel (Figure S2).

## Extraction of Single-Cell and Islet Level Data

Cell segmentation is essential to recover quantitative single-cell information from highly multiplexed images (Carpenter et al., 2006). We used supervised machine learning and computer vision algorithms to generate cell and islet segmentation masks, which represent pixels belonging

to the same cell or islet, respectively (Figure 1B, Figure S3 and STAR Methods) (Kamentsky et al., 2011; Sommer et al., 2011). Applying these masks over high-dimensional pictures allowed retrieval of phenotypic and functional marker expression, spatial information and neighborhood information. We also combined cell and islet masks to extract additional information, such as the distance from cells to the islet rim (Figure 1C-H). Although cell populations can be defined using clustering approaches, we sought a more accurate way to define cell types in our dataset and turned to supervised machine-learning approaches (Figure S3 and STAR Methods) (Sommer et al., 2011). We first trained a classifier to segregate cells into four main categories (i.e., islet, immune, exocrine, other) and then performed sub-classification within each category in order to identify individual cell types. Together, these approaches enabled extraction of a wide range of biological information that can be explored in downstream data analyses to gain deeper insights into cell phenotypes and tissue function.

**Evolution of Islet Cellular Composition and Architecture during T1D Progression**

Even within a single pancreas, islet size and cell type composition are highly heterogeneous (Brissova et al., 2005; Cabrera et al., 2006). Whether this heterogeneity influences T1D progression remains unknown. We, therefore, sought to determine how islet structure and cell type composition change when T1D progresses. The 1581 imaged islets displayed striking heterogeneity in terms of cell number and cell type composition (Figure 2A). We also observed large inter-donor variations (Figure 2B). As compared to non-diabetic controls, β cell fraction was reduced by 62% in donors with recent-onset T1D. Remarkably, two of the four samples from donors at T1D onset had a proportion of β cells approaching those observed in some of the non-diabetic individuals (nPOD cases 6414 and 6380 had 57% and 72% of the average β cell fraction in control donors, respectively). As expected, however, pancreata from donors with prolonged disease duration were almost entirely devoid of β cells. Next, we examined intra-pancreas heterogeneity to determine whether different regions of the same pancreas differed in cell type

composition. Within each pancreas, islet cellular composition was remarkably homogenous. We observed a significant difference in β cell loss between the pancreas body and tail in only one of the donors with recent disease onset (nPOD case 6380) (Figure 2C). Previous reports indicate that the head region of the pancreas is enriched in γ cells (Malaisse-Lagae et al., 1979; Brereton et al., 2015). We made a similar observation in the only pancreas head section analyzed (nPOD case 6264).

Next, we examined how cell type composition varied with islet size. We found that in non-diabetic donors, the percentage of β cells was highest in islets of intermediate size, and lowest in very small (< 10 cells) and very large (> 250 cells) islets (Figure 2D). The distribution of α cells exhibited the opposite trend, whereas δ cell fractions were fairly constant. We noticed a similar pattern in islets from recent-onset donors, whereas the few residual β cells found in donors with long-standing T1D were most often found isolated or in very small islets, in line with previous observations (Wasserfall et al., 2017).

Finally, we measured the distance of islet cell subsets to the islet rim and to blood vessels in order to evaluate human islet architecture. Because the risk of overestimating distances in two-dimensional images increases with the measured distance, we limited the range of our analyses to cells located within 25 µm of islet rims or blood vessels. We observed that in non-diabetic donors, α cells were preferentially located at the islet periphery than in the islet core, whereas β cells exhibited an opposite tropism (Figure 2E). Similarly, α cells were more frequently found along blood vessels than were β cells (Figure 2F). These findings support earlier observations (Bosco et al., 2010; Brereton et al., 2015). Further, we observed that this islet organization is globally conserved between non-diabetic and recent-onset T1D donors, whereas in islets from donors with long-standing T1D architecture is altered due to β cell loss (Figure 2E-F).

**Evolution of Islet Profiles during T1D Progression**

It would be ideal to observe changes of cell phenotypes and cell-cell interactions that take place inside islets during T1D progression. Unfortunately, the study of T1D pancreas pathology relies on samples collected post-mortem, only allowing for snapshot analysis. To generate a time resolved map of T1D pathogenesis, we sought to reconstruct islet evolution from cross-sectional data. To achieve this, we first determined islet expression profiles by quantifying abundances of 12 islet-expressed markers, averaged over the islet area. Hierarchical clustering of islet profiles distinguished non-diabetic from diseased donors but did not clearly separate recent-onset donors from those with long-standing disease (Figure S4A). To visualize individual islet profiles, we performed a dimensionality reduction analysis with tSNE (van der Maaten and Hinton, 2008). tSNE confirmed that islets from donors with or without T1D exhibited clearly distinct profiles (Figure 3A and Figure S4B), but the separation between islets from recent-onset and long-duration T1D donors was only partial. In particular, a large cluster composed of islets from donors with different disease durations was found (Figure 3A, circled in dotted blue line). These results indicated that islets from donors at very different T1D stages can have similar profiles.

To better understand how islet expression profiles change with disease progression, we performed a pseudotime analysis using the trajectory inference algorithm SCORPIUS (Figure 3B and Figure S4C) (Cannoodt et al., 2016; Saelens et al., 2018). This approach revealed that the abundance of β cell markers decreased with pseudotime progression (Figure 3C and Figure S4D). Strikingly, visualizing islet distribution over pseudotime revealed a bimodal distribution of islets from donors with recent T1D onset (Figure 3D, *left*). To analyze this observation in more detail, we calculated the density distributions in the assigned pseudotime for each stage (Figure 3D, *right*). We defined three pseudostages based on the intersections between these distributions, thereby allowing stratification of islets according to their individual expression profiles rather than on donor disease duration. Using this approach, islets from non-diabetic donors were distinct from islets from donors with T1D, but also about half of the islets from donors categorized as recent

onset exhibited the phenotype found in long-duration T1D (Figure 3D). We observed a similar bimodal distribution in samples from each of the four donors with recent-onset T1D (Figure S4E). Together these analyses revealed that islet profiles do not necessarily correlate with disease duration.

Because pseudotime was computed at the islet level rather than at the single-cell level, the observed decreased expression of β cell markers could be due to a loss of β cells or to downregulation of β cell markers in β cells or both. To separate these phenomena, we first compared the islet β cell fractions at the three pseudostages. The proportion of β cells decreased only slightly from pseudostage 1 to pseudostage 2, whereas pseudostage 3 was essentially composed of pseudo-atrophic islets, i.e. which are devoid of β cells (Figure 3E). In addition, we examined how islet shape changed with pseudostage progression. Islet extent (islet area divided by islet bounding box) and solidity (proportion of pixels in the islet convex hull that are also in the islet), two metrics that reflect shape regularity, were similar for pseudostages 1 and 2 and decreased for pseudostage 3 (Figure 3F). This reflects altered islet shape at pseudostage 3, likely because of β cell destruction.

We then examined how the expression of β cell markers evolved with pseudotime. We assessed the abundance of β cell markers in the β cells of each islet as a function of pseudotime. This approach revealed that expression of four β cell markers (INS, PIN, IAPP, and PTPRN) was strongly downregulated between pseudostages 1 and 2 but remained relatively stable between pseudostages 2 and 3 (Figure 3G and Figure S5A). By contrast, the expression of β cell transcription factors, PDX1 and NKX6-1, and pan-endocrine markers, SYP and CD99, did not vary substantially through the three pseudostages. Together, these results indicate that progression from pseudostage 1 to 2 is driven by a downregulation of β cell-specific markers, while progression to pseudostage 3 reflects β cell death. Similar results were obtained using Monocle2 (Qiu et al., 2017) instead of SCORPIUS for pseudotime analysis (Figure S5B-G), indicating that our results are independent of the pseudotime mapping algorithm used. We

194 performed similar analyses at the β cell level. Despite heterogeneity, β cells from non-diabetic
195 controls and donors with T1D were largely separated by both hierarchical clustering and tSNE
196 and had limited pseudotime overlap (Figure S5H-K). As in the islet-level analysis, this separation
197 was mainly driven by a relative decrease in the abundance of INS, PIN, IAPP and PTPRN (Figure
198 S5L). In summary, these findings indicate that islet evolution during T1D progression can be
199 reconstructed from cross-sectional data and suggest that, at the islet level, alteration of the β cell
200 phenotype precedes β cell destruction.
201
202 **Tc and Th Cells are Simultaneously Recruited to β Cell-Rich Islets at T1D Onset**
203 Autoimmunity is thought to be the driving force behind β cell death in T1D (Atkinson et al., 2014;
204 Boldison and Wong, 2016). We therefore explored the evolution of immune cell composition
205 through disease duration. We used supervised machine learning to identify the main immune cell
206 types in our dataset: cytotoxic T cells (Tc, $CD3^+CD8^+CD45RA^-$), naïve (possibly EMRA) Tc cells
207 (naïve Tc, $CD3^+CD8^+CD45RA^+$), helper T cells (Th, $CD3^+CD4^+$), B cells ($CD20^+$),
208 monocytes/macrophages (MΦ, $CD45^+CD68^+$), and neutrophils (Neutr., $MPO^+$). In addition,
209 remaining $CD45^+$ or $CD45RA^+$ cells, to which no specific cell type could be attributed, were
210 classified as “other”. Overall, T cells were more abundant in donors with recent-onset T1D and
211 the number of B cells was very low in most pancreata, except for one donor with recent-onset
212 T1D (nPOD case 6228) (Figure 4A). We then measured the density of each immune cell type
213 (i.e., number of cells per $mm^2$) across T1D duration. All measured immune cell types were more
214 abundant in recent-onset than in control donors (Figure 4B). In long-duration T1D donors, MΦ
215 and neutrophil densities were elevated relative to donors without T1D, whereas Tc and Th cell
216 abundances were decreased compared to recent-onset donors but remained higher than in
217 donors without T1D (Figure 4B and S6A). We then tested whether immune cell densities in islets
218 differed from those in the surrounding exocrine tissue. Strikingly, the density (cells per $mm^2$) of
219 immune cells was lower in islets than in the exocrine compartment for all immune cell types except

B cells at all disease stages (Figure 4C). Yet, while immune cell densities never exceeded 20 cells per $mm^2$ in the exocrine tissue, a few islets exhibited much higher values. Next, we investigated whether positions of immune cells relative to islets varied but did not observe an accumulation of immune cells at islet peripheries (Figure 4D). The exception to this was observed in a donor with recent-onset T1D (nPOD case 6414) with an accumulation of Tc and Th cells around the islet periphery (Figure S6B). Together, these results indicate that more immune cells are found in pancreata from donors with T1D than in non-diabetic controls. Most of these immune cells are not directly associated with islets, however.

To further explore interactions between islets and immune cells in T1D, we sought to correlate islet pseudostage information, which reflects the islet marker expression profile, with our immune cell data. We counted the number of immune cells associated with each islet (i.e., the number of immune cells located either inside the islet or within 20 µm of the islet rim) and calculated the fraction of islets with immune cell infiltration at different disease stages (Figure 4E and Figure S6C). Most islets from non-diabetic controls and donors with long-duration T1D had no or few associated immune cells. By contrast, around half of the islets from donors with recent-onset T1D had six associated immune cells or more. Strikingly, insulitis (> 15 associated immune cells) was present in over 30% of β cell-rich (pseudostage 2) islets from recent-onset donors, but in less than 10% of β cell-depleted (pseudostage 3) islets from the same donors. We then examined how immune cell numbers varied with pseudostage progression. Islet-associated Tc and Th cells were more abundant in pseudostage 2 islets but these numbers decreased in pseudostage 3 islets from recent-onset T1D donors and further decreased in pseudostage 3 islets from donors with long-duration T1D, suggesting that T cells progressively leave islets after β cell destruction (Figure 4F). Together, these results indicated that the number of islet-associated T cells depends on both disease duration (recent-onset versus long-duration) and the islet profile (presence of surviving β cells).

We observed that Tc and Th cell numbers followed similar trajectories through pseudotime (Figure 4G), suggesting that these cells are recruited simultaneously to individual islets in T1D. This was confirmed by the positive correlation between the numbers of Tc and Th cells associated with individual islets, in particular at pseudostage 2 (Figure 4H). These findings indicated that the immune-mediated attack on β cells involves both Tc and Th cells, is maximal around the time of T1D onset, and focuses on islets that retain a high proportion of β cells. Moreover, our results show that pseudotime analysis based on islet expression profiles can be meaningfully combined with immune cell data to recreate the dynamics of interactions between islets and immune cells through T1D duration.

**Neighborhood Analysis Reveals Dynamic Changes in Cell-Cell Interactions in T1D**

In health and disease, tissue function depends on interactions between different cell types. This is also the case in the pancreas: Normal islet function depends on paracrine interactions between islet cells, and T1D progression is determined by interactions between immune and β cells. Understanding how cell-cell interactions change from one disease stage to the other is, therefore, key to a better understanding of T1D. To systematically probe interactions between cell types, we performed a large-scale neighborhood analysis (Schapiro et al., 2017). We measured, for each image, significant association or avoidance according to spatial proximity of all cell type pairs in our dataset (Figure 5A). Hierarchical clustering of individual images based on cell-cell interactions revealed a clear separation between images containing pseudostage 3 islets and those containing islets at pseudostages 1 or 2. This separation was essentially caused by β cell destruction, as illustrated by the rarity of significant association between β cells and other cell types in images containing pseudostage 3 islets (Figure 5A, green rectangle). This result confirmed that islet structure is maintained between pseudostage 1 and pseudostage 2 islets but is altered in pseudostage 3 islets. We then focused specifically on islets and compared the frequency of interactions between cell types at each pseudostage (Figure 5B). As expected, we observed

frequent association between islet cells (Figure 5B, green rectangles), but interactions involving β cells were strongly reduced or absent in pseudostage 3 islets, as a result of β cell loss. Association between immune cells was also frequent, in particular at pseudostages 2 and 3 (Figure 5B, magenta rectangles). By contrast, islet and immune cells essentially remained isolated from each other at all disease stages, confirming our previous observation that immune cells are rarely found within islets.

Cytotoxic and helper T cells are thought to be directly involved in the destruction of β cells in T1D (Boldison and Wong, 2016). Yet, our global neighborhood analysis did not detect association between T cells and β cells, even in donors with recent-onset T1D, where the rate of β cell death and islet infiltration are maximal. We, therefore, sought to study specifically the evolution of interactions between β and T cells through disease progression. First, we counted how often β cells were associated with Tc, respectively Th cells. This number remained extremely low in all islets but was highest for β cells from pseudostage 2 islets, i.e. β cell-rich islets from donors with recent-onset T1D (Figure 5C). Conversely, T cells were more often associated with β cells located in pseudostage 2 islets (Figure 5D). Next, we calculated for each islet the fraction of β cells associated with either Tc or Th cells. Again, more islets displayed such contacts at pseudostage 2 (Figure 5E). Even in those islets, though, the percentage of β cells associated with T cells was rarely above 10%. Conversely, the fraction of T cells associated with β cells was also higher in pseudostage 2 islets (Figure 5F). The small fraction of β cells in contact with T cells likely explains why our global neighborhood analysis did not allow detecting those associations. Together with the results of our immune cell analysis, these results suggested that not only pseudostage 2 islets have more associated T cells, but also that, in those islets, T cells contact β cells more frequently. Nevertheless, the frequency of interactions between β and T cells remained very low at all disease stages.

## DISCUSSION

Here we used highly multiplexed imaging of human pancreas sections by IMC to generate a comprehensive map of T1D progression. Analysis of islet cell composition showed that two donors with recent-onset T1D had a proportion of β cells in islets similar to that observed in non-diabetic controls (Figure 2B). The discrepancy with β cell fractions usually reported can be, at least in part, explained by the presence of insulin-negative β cells, which we detected by co-expression of Pdx1 and Nkx6.1. These β cells with altered phenotypes are not detected when β cell identification relies exclusively on insulin (Rodriguez-Calvo et al., 2017; Wasserfall et al., 2017). The question remains, however, how patients with such high numbers of remaining β cells develop clinical symptoms of T1D. We found that roughly half of the islets from donors with recent-onset T1D retained a “normal” fraction of β cells with an unaltered islet structure (Figure 3E). The β cells in these islets, however, exhibited reduced expression of β cell markers as compared to β cells from healthy control islets (Figure 3G). This altered phenotype may be a consequence of stress and/or increased metabolic demand or, potentially, may allow escape from detection by the immune system (Rui et al., 2017). This finding is crucial from a therapeutic point of view because the presence of a high number of surviving β cells at T1D onset implies that if factors driving disease progression could be halted or slowed these cells might have the opportunity to regain functionality.

Much of our knowledge regarding T1D pancreas pathology has resulted from analyses of sections collected from deceased pancreas donors, and the lack of sampling over the course of the disease has clearly hampered study of this disorder. We show here that performing pseudotime ordering at the islet level represents a powerful method to reconstruct time trajectories from snapshot data, and studies such as ours may overcome the sample limitation issues. In particular, we investigated the dynamics of immune cell recruitment around T1D-affected islets and found that the number of islet-associated T cells depends on both disease

stage and islet profile. In addition, we observed simultaneous recruitment of Tc and Th cells to individual islets before β cell destruction in subjects already diagnosed with T1D. This result confirms that these cell types form a destructive immune motif that plays a pivotal role in β cell demise. Finally, our analyses indicate that immune cells are rarely in direct contact with islet cells. This could be explained by the fact that infiltrating immune cells are more often located at the islet periphery (peri-insulitis), than inside islets (intra-insulitis) (Pugliese, 2016). The position of β cells, which are rarely located in the outer islet layer (Figure 2E), may represent an additional barrier. Finally, the chronic nature of the disease, with β cell destruction taking place over long-time periods, is consistent with a model in which contacts between T and β cells are relatively short and infrequent, making their detection in fixed tissue sections difficult.

For this first effort toward analysis of human pancreata using highly multiplexed imaging, we designed a broad antibody panel that enabled discrimination of the main pancreatic and immune cell types and selected cases that represented short and long duration T1D. We envision that future studies will attempt to address specific questions with tailored antibody panels and higher numbers of donors in order to increase the statistical power, to better capture heterogeneity among donors, and to explore other patient-related parameters known to influence T1D progression, such as age. A number of questions regarding T1D development remain open. We could not determine, for instance, whether recruitment of immune cells to pancreatic islets precedes or follows downregulation of insulin and other β cell markers. Because β cell phenotypes are already altered in recently diagnosed donors, determining the cause of this alteration and the underlying mechanisms will require studying samples from pre-diabetic subjects.

The techniques and concepts described in the current study, together with the co-submitted manuscript (Wang et al., 2018), will open new avenues for the exploration of T1D pancreas pathology and will help to address the crucial questions that still surround the disorder. Moreover, the approaches described herein should be applicable to the study of other diseases and will be especially valuable for deciphering complex cellular interactions.

## Limitations of study

Some limitations remain when IMC is used for analysis of pancreas tissues. First, all results are a function of the selected antibodies. Antibodies used in this study were thoroughly validated (STAR Methods). In IMC, antigens are most often directly detected with primary antibodies so options for signal amplification are limited. Moreover, due to the multiplexed nature of IMC, a single staining protocol must be used, whereas in IF or IHC the conditions can be optimized for each antibody. Conjugation can also affect the performance of some antibodies. New antibody conjugation methods will become available in the near future (Allo et al., 2018). Second, the area that can be imaged by IMC is constrained by acquisition speed. To overcome this caveat, we used IF to select areas of interest for IMC analysis. Yet, the number of slides that can be imaged remains limited. In this study, we have analyzed two sections per donor, but we have acquired a large number of islets per section, such that variations related to the sectioning plane should average out. In this regard, we note that islet cellular compositions were globally similar between sections from different anatomical regions of the same pancreas. Third, among the most challenging processes in multiplexed image analysis is cell segmentation. Because cell borders are not always clearly defined and because individual pixels may contain information from more than one cell (Schapiro et al., 2017), tissue imaging data are noisier than what is typically obtained with suspension analysis methods. We have, therefore, implemented supervised machine learning for cell type attribution to overcome this challenge. These computational pipelines and new tools to be developed in the future will lead to further improvements in the quality of IMC-generated data.

## ACKNOWLEDGEMENTS

We thank Amanda L. Posgai for editing the manuscript and James Ross for help with antibody testing. This research was performed with the support of the Network for Pancreatic Organ Donors with Diabetes (nPOD), a collaborative T1D research project sponsored by JDRF. Organ Procurement Organizations (OPO) partnering with nPOD to provide research resources are listed at http://www.jdrfnpod.org//for-partners/npod-partners. We thank the Center for Microscopy and Image Analysis, University of Zurich, for access to fluorescence microscopes and virtual machines. This research was funded by NIH grants (DK108132 and AI42288). The pancreatic tissues were obtained through funding by the JDRF and the Leona M. and Harry B. Helmsley Charitable Trust. D.S. was supported by the BioEntrepreneur-Fellowship of the University of Zurich (BIOEF-17-001).

## AUTHOR CONTRIBUTIONS

Conceptualization, N.D., H.S.N., F.T., P.L.H., M.A.A., and B.B; Methodology, N.D., S.E., and C.H.W.; Software, V.R.T.Z., N.D., and D.S.; Investigation, N.D. and S.E.; Resources, I.K. and M.A.A.; Formal analysis, N.D.; Writing, N.D., M.A.A. and B.B.; Visualization, N.D. and B.B.; Funding acquisition, B.B., M.A.A., and P.L.H.

## DECLARATION OF INTERESTS

The authors declare no competing interests.

# REFERENCES


Allo, B., Lou, X., Bouzekri, A., and Ornatsky, O. (2018). Clickable and High-Sensitivity Metal-Containing Tags for Mass Cytometry. Bioconjug Chem *29*, 2028-2038.

Angelo, M., Bendall, S.C., Finck, R., Hale, M.B., Hitzman, C., Borowsky, A.D., Levenson, R.M., Lowe, J.B., Liu, S.D., and Zhao, S., et al. (2014). Multiplexed ion beam imaging of human breast tumors. Nat Med *20*, 436-442.

Atkinson, M.A., Eisenbarth, G.S., and Michels, A.W. (2014). Type 1 diabetes. Lancet *383*, 69-82.

Bodenmiller, B. (2016). Multiplexed Epitope-Based Tissue Imaging for Discovery and Healthcare Applications. Cell Syst *2*, 225-238.

Boldison, J., and Wong, F.S. (2016). Immune and Pancreatic β Cell Interactions in Type 1 Diabetes. Trends Endocrinol Metab *27*, 856-867.

Bosco, D., Armanet, M., Morel, P., Niclauss, N., Sgroi, A., Muller, Y.D., Giovannoni, L., Parnaud, G., and Berney, T. (2010). Unique arrangement of alpha- and beta-cells in human islets of Langerhans. Diabetes *59*, 1202-1210.

Brereton, M.F., Vergari, E., Zhang, Q., and Clark, A. (2015). Alpha-, Delta- and PP-cells. Are They the Architectural Cornerstones of Islet Structure and Co-ordination? J Histochem Cytochem *63*, 575-591.

Brissova, M., Fowler, M.J., Nicholson, W.E., Chu, A., Hirshberg, B., Harlan, D.M., and Powers, A.C. (2005). Assessment of human pancreatic islet architecture and composition by laser scanning confocal microscopy. J Histochem Cytochem *53*, 1087-1097.

Cabrera, O., Berman, D.M., Kenyon, N.S., Ricordi, C., Berggren, P.-O., and Caicedo, A. (2006). The unique cytoarchitecture of human pancreatic islets has implications for islet cell function. Proc Natl Acad Sci U S A *103*, 2334-2339.

Campbell-Thompson, M., Fu, A., Kaddis, J.S., Wasserfall, C., Schatz, D.A., Pugliese, A., and Atkinson, M.A. (2016). Insulitis and β-Cell Mass in the Natural History of Type 1 Diabetes. Diabetes *65*, 719-731.

Campbell-Thompson, M., Wasserfall, C., Kaddis, J., Albanese-O'Neill, A., Staeva, T., Nierras, C., Moraski, J., Rowe, P., Gianani, R., and Eisenbarth, G., et al. (2012a). Network for Pancreatic Organ Donors with Diabetes (nPOD). Developing a tissue biobank for type 1 diabetes. Diabetes Metab Res Rev *28*, 608-617.

Campbell-Thompson, M.L., Montgomery, E.L., Foss, R.M., Kolheffer, K.M., Phipps, G., Schneider, L., and Atkinson, M.A. (2012b). Collection protocol for human pancreas. J Vis Exp, e4039.

Cannoodt, R., Saelens, W., Sichien, D., Tavernier, S., Janssens, S., Guilliams, M., Lambrecht, B.N., Preter, K. de, and Saeys, Y. (2016). SCORPIUS improves trajectory inference and identifies novel modules in dendritic cell development. bioRxiv, doi: 10.1101/123456.

Carpenter, A.E., Jones, T.R., Lamprecht, M.R., Clarke, C., Kang, I.H., Friman, O., Guertin, D.A., Chang, J.H., Lindquist, R.A., and Moffat, J., et al. (2006). CellProfiler. Image analysis software for identifying and quantifying cell phenotypes. Genome Biol *7*, R100.

Chen, C., Cohrs, C.M., Stertmann, J., Bozsak, R., and Speier, S. (2017). Human beta cell mass and function in diabetes. Recent advances in knowledge and technologies to understand disease pathogenesis. Mol Metab *6*, 943-957.

Chen, K.H., Boettiger, A.N., Moffitt, J.R., Wang, S., and Zhuang, X. (2015). RNA imaging. Spatially resolved, highly multiplexed RNA profiling in single cells. Science *348*, aaa6090.

Chevrier, S., Crowell, H.L., Zanotelli, V.R.T., Engler, S., Robinson, M.D., and Bodenmiller, B. (2018). Compensation of Signal Spillover in Suspension and Imaging Mass Cytometry. Cell Syst, doi: 10.1016/j.cels.2018.02.010.

Coppieters, K.T., Dotta, F., Amirian, N., Campbell, P.D., Kay, T.W.H., Atkinson, M.A., Roep, B.O., and Herrath, M.G. von (2012). Demonstration of islet-autoreactive CD8 T cells in insulitic lesions from recent onset and long-term type 1 diabetes patients. J Exp Med *209*, 51-60.

Foulis, A.K., and Stewart, J.A. (1984). The pancreas in recent-onset type 1 (insulin-dependent) diabetes mellitus. Insulin content of islets, insulitis and associated changes in the exocrine acinar tissue. Diabetologia *26*, 456-461.

Gepts, W. (1965). Pathologic Anatomy of the Pancreas in Juvenile Diabetes Mellitus. Diabetes *14*, 619-633.

Gerdes, M.J., Sevinsky, C.J., Sood, A., Adak, S., Bello, M.O., Bordwell, A., Can, A., Corwin, A., Dinn, S., and Filkins, R.J., et al. (2013). Highly multiplexed single-cell analysis of formalin-fixed, paraffin-embedded cancer tissue. Proc Natl Acad Sci U S A *110*, 11982-11987.

Gianani, R., Campbell-Thompson, M., Sarkar, S.A., Wasserfall, C., Pugliese, A., Solis, J.M., Kent, S.C., Hering, B.J., West, E., and Steck, A., et al. (2010). Dimorphic histopathology of long-standing childhood-onset diabetes. Diabetologia *53*, 690-698.

Giesen, C., Wang, H.A.O., Schapiro, D., Zivanovic, N., Jacobs, A., Hattendorf, B., Schüffler, P.J., Grolimund, D., Buhmann, J.M., and Brandt, S., et al. (2014). Highly multiplexed imaging of tumor tissues with subcellular resolution by mass cytometry. Nat Methods *11*, 417-422.

Goltsev, Y., Samusik, N., Kennedy-Darling, J., Bhate, S., Hale, M., Vazquez, G., Black, S., and Nolan, G.P. (2018). Deep Profiling of Mouse Splenic Architecture with CODEX Multiplexed Imaging. Cell *174*, 968-981.e15.

Gut, G., Herrmann, M.D., and Pelkmans, L. (2018). Multiplexed protein maps link subcellular organization to cellular states. Science *361*.

Kamentsky, L., Jones, T.R., Fraser, A., Bray, M.-A., Logan, D.J., Madden, K.L., Ljosa, V., Rueden, C., Eliceiri, K.W., and Carpenter, A.E. (2011). Improved structure, function and compatibility for CellProfiler. Modular high-throughput image analysis software. Bioinformatics *27*, 1179-1180.

Ke, R., Mignardi, M., Pacureanu, A., Svedlund, J., Botling, J., Wählby, C., and Nilsson, M. (2013). In situ sequencing for RNA analysis in preserved tissue and cells. Nat Methods *10*, 857-860.

Lee, J.H., Daugharthy, E.R., Scheiman, J., Kalhor, R., Yang, J.L., Ferrante, T.C., Terry, R., Jeanty, S.S.F., Li, C., and Amamoto, R., et al. (2014). Highly multiplexed subcellular RNA sequencing in situ. Science *343*, 1360-1363.

Lin, J.-R., Fallahi-Sichani, M., and Sorger, P.K. (2015). Highly multiplexed imaging of single cells using a high-throughput cyclic immunofluorescence method. Nat Commun *6*, 8390.

Malaisse-Lagae, F., Stefan, Y., Cox, J., Perrelet, A., and Orci, L. (1979). Identification of a lobe in the adult human pancreas rich in pancreatic polypeptide. Diabetologia *17*, 361-365.

Marchetti, P., Suleiman, M., and Marselli, L. (2018). Organ donor pancreases for the study of human islet cell histology and pathophysiology. A precious and valuable resource. Diabetologia *61*, 770-774.

Meier, J.J., Bhushan, A., Butler, A.E., Rizza, R.A., and Butler, P.C. (2005). Sustained beta cell apoptosis in patients with long-standing type 1 diabetes. Indirect evidence for islet regeneration? Diabetologia *48*, 2221-2228.

Pugliese, A. (2016). Insulitis in the pathogenesis of type 1 diabetes. Pediatr Diabetes *17 Suppl 22*, 31-36.

Qiu, X., Mao, Q., Tang, Y., Wang, L., Chawla, R., Pliner, H.A., and Trapnell, C. (2017). Reversed graph embedding resolves complex single-cell trajectories. Nat Methods *14*, 979-982.

Rodriguez-Calvo, T., Suwandi, J.S., Amirian, N., Zapardiel-Gonzalo, J., Anquetil, F., Sabouri, S., and Herrath, M.G. von (2015). Heterogeneity and Lobularity of Pancreatic Pathology in Type 1 Diabetes during the Prediabetic Phase. J Histochem Cytochem *63*, 626-636.

Rodriguez-Calvo, T., Zapardiel-Gonzalo, J., Amirian, N., Castillo, E., Lajevardi, Y., Krogvold, L., Dahl-Jørgensen, K., and Herrath, M.G. von (2017). Increase in Pancreatic Proinsulin and Preservation of β-Cell Mass in Autoantibody-Positive Donors Prior to Type 1 Diabetes Onset. Diabetes *66*, 1334-1345.

Rui, J., Deng, S., Arazi, A., Perdigoto, A.L., Liu, Z., and Herold, K.C. (2017). β Cells that Resist Immunological Attack Develop during Progression of Autoimmune Diabetes in NOD Mice. Cell Metab *25*, 727-738.

Saelens, W., Cannoodt, R., Todorov, H., and Saeys, Y. (2018). A comparison of single-cell trajectory inference methods. Towards more accurate and robust tools. bioRxiv, doi: 10.1101/276907.

Schapiro, D., Jackson, H.W., Raghuraman, S., Fischer, J.R., Zanotelli, V.R.T., Schulz, D., Giesen, C., Catena, R., Varga, Z., and Bodenmiller, B. (2017). histoCAT. Analysis of cell phenotypes and interactions in multiplex image cytometry data. Nat Methods *14*, 873-876.

Schindelin, J., Arganda-Carreras, I., Frise, E., Kaynig, V., Longair, M., Pietzsch, T., Preibisch, S., Rueden, C., Saalfeld, S., and Schmid, B., et al. (2012). Fiji. An open-source platform for biological-image analysis. Nat Methods *9*, 676-682.

Schubert, W., Bonnekoh, B., Pommer, A.J., Philipsen, L., Böckelmann, R., Malykh, Y., Gollnick, H., Friedenberger, M., Bode, M., and Dress, A.W.M. (2006). Analyzing proteome topology and function by automated multidimensional fluorescence microscopy. Nat Biotechnol *24*, 1270-1278.

Schulz, D., Zanotelli, V.R.T., Fischer, J.R., Schapiro, D., Engler, S., Lun, X.-K., Jackson, H.W., and Bodenmiller, B. (2018). Simultaneous Multiplexed Imaging of mRNA and Proteins with Subcellular Resolution in Breast Cancer Tissue Samples by Mass Cytometry. Cell Syst *6*, 25-36.e5.

Sommer, C., Straehle, C., Kothe, U., and Hamprecht, F.A. (2011). Ilastik. Interactive learning and segmentation toolkit. In 2011 8th IEEE International Symposium on Biomedical Imaging (Piscataway: IEEE), pp. 230–233.

van der Maaten, L., and Hinton, G. (2008). Visualizing Data using t-SNE. J. Mach. Learn. Res. *9*, 2579-2605.

Wang, Y.J., Traum, D., Schug, J., Gao, L., Liu, C., HPAP Consortium, Atkinson, M.A., Powers, A.C., Feldman, M.D., and Naji, A., et al. (2018). Multiplexed *in Situ* Imaging Mass Cytometry Analysis of the Human Endocrine Pancreas and Immune System in Type 1 Diabetes. Cell Metab.

Wasserfall, C., Nick, H.S., Campbell-Thompson, M., Beachy, D., Haataja, L., Kusmartseva, I., Posgai, A., Beery, M., Rhodes, C., and Bonifacio, E., et al. (2017). Persistence of Pancreatic Insulin mRNA Expression and Proinsulin Protein in Type 1 Diabetes Pancreata. Cell Metab *26*, 568-575.e3.

Zrazhevskiy, P., and Gao, X. (2013). Quantum dot imaging platform for single-cell molecular profiling. Nat Commun *4*, 1619.

## MAIN FIGURE LEGENDS

**Figure 1. Acquisition of Single-Cell and Islet Level Data by IMC**

**A.** IMC workflow. A laser ablates the tissue spot-by-spot, generating clouds of particles that are atomized and ionized in an inductively coupled plasma before analysis by mass cytometry. Based on ion cloud composition, an image of the ablated area is created for each measured marker.

**B.** IMC images, here represented by a combination of proinsulin (magenta), glucagon (cyan), and somatostatin (yellow) (top), were segmented into cells. The cell mask is shown as a white overlay (bottom).

**C.** Marker expression was measured by applying cell masks onto IMC images (left). Protein abundance in single cells can be visualized using tSNE (right).

**D.** Imaged cells were classified into cell types (left). Cells were first divided into four categories: islet (red), exocrine (blue), immune (green), and “other” (yellow) (left). Each category was then subdivided into cell types. Islet cells were classified as α (cyan), β (magenta), δ (yellow), or γ (red) cells (center). This allowed determination of islet cellular composition (right).

**E.** Cell masks enabled retrieval of spatial data, such as cell area (left). Neighborhood information (center) was used to systematically analyze cell-cell interactions (right).

**F.** The expression of endocrine cell markers, such as synaptophysin (red) (top), was used to identify islets and generate islet masks (white overlay, bottom).

**G.** By combining cell and islet masks, each cell was related to the islet to which it belongs (left). The distance of cells to the islet rim was also measured (center), allowing comparison of cell positions relative to islets (right).

**H.** Spatial information (left) and protein abundance (center) were measured at the islet level using islet masks. Islet level data were used to perform pseudotime analyses (right).

Scale bars: 100 µm.

**Figure 2. IMC Exploration of Islet Heterogeneity**

**A.** Cell type composition of the 1581 islets (≥ 10 islet cells) captured in our dataset. Each stacked bar represents a single islet with colors indicating β (red, $n = 56,594$), α (light red, $n = 101,592$), δ (blue, $n = 18,833$), and γ (light blue, $n = 3721$) cells.

**B.** Average islet cell type fraction for each of the 12 donors in our dataset.

**C.** Average islet cell type fraction per pancreas section. The region of origin of each section is indicated on the x-axis. Significant *P* values for comparison of β cell fractions between sections of the same pancreas are indicated.

**D.** Average islet cell type fraction versus islet size. For each bin size, β cell fraction was compared to the average β cell fraction for the central bin (35-100 cells).

**E.** Islet cell type fractions as a function of distance to islet rim. Cell types β (red, $n = 39,557$), α (light red, $n = 73,174$), δ (blue, $n = 14,396$), γ (light blue, $n = 3431$) cells. Bin sizes, 5 μm. The leftmost bin represents cells located within 5 μm of the islet rim and increasing bin numbers indicate cells located closer and closer to the islet center.

**F.** Islet cell type fractions as a function of distance to blood vessels. Cell types: β (red, $n = 42,948$), α (light red, $n = 89,782$), δ (blue, $n = 16,114$), γ (light blue, $n = 2734$) cells. Bin sizes, 5 μm. The leftmost bin represents cells located within 5 μm of the blood vessel, and increasing bin numbers represent cells located farther and farther away.

*, $P < 0.01$; **, $P < 0.001$; ***, $P < 0.0001$ for β cell fractions; †, $P < 0.01$; ††, $P < 0.001$; †††, $P < 0.0001$ for α cell fractions (Mann-Whitney *U* test with Holm adjustment). Error bars, SEM.

**Figure 3. Evolution of Islet Profiles with T1D Progression**

**A.** tSNE map representing the expression profiles of 1494 islets (≥ 15 cells) from 12 donors at different stages of T1D (one circle = one islet, 90 to 155 islets per donor, see also Figure S4B). The dotted blue circle indicates a cluster composed of islets from donors with different disease durations.

**B.** Pseudotime analysis of islet expression profiles using SCORPIUS. Islets, represented by circles, were first projected into a two-dimensional space (Components 1 and 2). A trajectory, represented by the black curve, was then inferred in the reduced space. Pseudotime was measured by projecting the islets onto the trajectory (see also Figure S4C-D).

**C.** Heatmap showing expression of islet markers with columns representing islets arranged according to pseudotime progression.

**D.** Violin plots showing islet distribution over pseudotime for the three disease stages (left). Pseudostages are indicated in blue and are defined based on the density distribution of islets for each disease stage (right). The percentage of islets in each stage and pseudostage is indicated in blue. Horizontal blue lines, defined by the intersections of islet density distributions, indicate pseudostage separations (see also Figure S4E).

**E.** Islet β cell fraction for each pseudostage. Pseudostage 1, $n = 514$ islets; pseudostage 2, $n = 289$ islets; pseudostage 3, $n = 691$ islets.

**F.** Islet extent and solidity measured for each pseudostage. For both metrics, a decrease indicates a more concave or irregular shape.

**G.** Evolution of β cell marker expression in β cells through pseudostages. Expression levels were measured in single β cells and averaged for each islet (see also Figure S5A). Pseudostage 1, $n = 38,479$ β cells from 514 islets; pseudostage 2, $n = 16,103$ β cells from 289 islets; pseudostage 3, $n = 618$ β cells from 691 islets.

Pairwise comparisons of the three pseudostages: *, $P < 0.01$; **, $P < 0.001$; ***, $P < 0.0001$, *n.s.*, not significant (Mann-Whitney *U* test with Holm adjustment).

**Figure 4. Dynamics of Immune Cell Recruitment during T1D Progression**

**A.** Distribution of immune cell types per donor and T1D stage. Number of cells analyzed: Tc, 15,367; Naïve Tc, 890; Th, 5417; B, 869; MΦ, 16,021; Neutr., 20,800; Other, 10,299.

**B.** Density (cells per $mm^2$) of immune cell types in pancreata from controls and donors with T1D (see also Figure S6A). *P* values, pairwise comparisons of T1D stages.

**C.** Immune cell densities inside islets (green lining) and in the exocrine tissue (blue lining) in controls and donors with T1D. *P* values, comparison of densities in islets versus exocrine tissue.

**D.** Average number of immune cells over binned distance to islet rim (see also Figure S6B). Bin size, 10 µm. Negative and positive values represent bins located outside and inside islets, respectively. The dotted vertical lines indicate the islet rim. B cells were not numerous enough to be meaningfully plotted. Error bars, SEM.

**E.** Fraction of islets containing given numbers of associated immune cells (inside the islet or within 20 µm of the islet rim), in function of pseudostage (see also Figure S6C).

**F.** Number of immune cells associated with islets at different pseudostages. Number of cells analyzed: Tc, 3533; Naïve Tc, 264; Th, 1309; B, 165; MΦ, 1915; Neutr., 2234; Other, 1868. *P* values, comparison of immune cell numbers for consecutive pseudostages.

**G.** Number of Tc (red) and Th (blue) cells associated with individual islets plotted versus islet pseudotime. Curves: smoothed conditional means (local polynomial regression fitting), grey areas: 95% confidence intervals.

**H.** Number of Tc and Th cells per islet at different pseudostages. Pearson correlations are indicated, *P* values were $< 1e^{-12}$ for the four pseudostages.

*, $P < 0.01$; **, $P < 0.001$; ***, $P < 0.0001$, *n.s.*, not significant (Mann-Whitney *U* test with Holm adjustment).

**Figure 5. Neighborhood Analysis Reveals Dynamic Changes in Cell-Cell Interactions in T1D**

**A.** Heatmap showing interactions between all cell type pairs (columns) for each individual image in our dataset (rows). Colors indicate significant ($P < 0.01$) cell type association (red) or avoidance (blue). Rows are ordered by hierarchical clustering. Non-present and non-significant interactions

are indicated in white. The green rectangle highlights interactions between β cells and other cell types in images containing pseudostage 3 islets.

**B.** Frequency of cell-cell interactions in islets and in the 20 µm surrounding area for each pseudostage. Colors indicate the percentage of donors that display significant association (red) or avoidance (blue) between two cell types. Green rectangles indicate interactions between islet cells and magenta rectangles indicate interactions between immune cells.

**C.** Average number of interactions per β cell, with either Tc or Th cells, averaged by islet. Only islets containing at least one β cell were considered.

**D.** Average number of interactions per Tc or Th cell with β cells, averaged by islet. Only islets with at least one associated T cell were considered.

**E.** Fraction of islets showing association between β and T cells, in function of the percentage of β cells associated with T cells.

**F.** Fraction of islets showing association between T and β cells, in function of the percentage of T cells associated with β cells.

*, $P < 0.01$; **, $P < 0.001$; ***, $P < 0.0001$, *n.s.*, not significant (Mann-Whitney *U* test with Holm adjustment).

# MAIN TABLES

| Compartment | Short name | Antigen | Main target cells | Metal tag |
|---|---|---|---|---|
| Pancreas | INS | Insulin | β | $^{141}$Pr |
| | PIN | Proinsulin | β | $^{154}$Sm |
| | GCG | Glucagon | α | $^{156}$Gd |
| | SST | Somatostatin | δ | $^{159}$Tb |
| | PPY | Pancreatic polypeptide | γ | $^{153}$Eu |
| | NKX6-1 | Nkx6.1 | β | $^{169}$Tm |
| | PDX1 | Pdx1 | β, δ, ductal | $^{158}$Gd |
| | IAPP | Amylin | β | $^{167}$Er |
| | PCSK2 | Proprotein convertase 2 | α | $^{144}$Nd |
| | SYP | Synaptophysin | Endocrine | $^{160}$Gd |
| | CD99 | CD99 | Endocrine | $^{145}$Nd |
| | SLC2A1 | Glucose transporter 1 | Endocrine | $^{148}$Nd |
| | PTPRN | Receptor-type tyrosine-protein phosphatase-like N | Endocrine | $^{174}$Yb |
| | AMY2A | Pancreatic amylase | Acinar | $^{150}$Nd |
| | KRT19 | Cytokeratin 19 | Ductal | $^{161}$Dy |
| | CD44 | CD44 | Exocrine | $^{143}$Nd |
| Immune | CD45 | CD45 | Immune | $^{162}$Dy |
| | CD45RA | CD45RA | Immune | $^{164}$Dy |
| | CD3e | CD3ε | T | $^{152}$Sm |
| | CD4 | CD4 | Helper T | $^{171}$Yb |
| | CD8a | CD8a | Cytotoxic T | $^{165}$Ho |
| | CD20 | CD20 | B | $^{149}$Sm |
| | CD68 | CD68 | Monocytes, macrophages | $^{146}$Nd |
| | MPO | Myeloperoxidase | Neutrophils | $^{147}$Sm |
| | FOXP3 | Forkhead box P3 | Regulatory T | $^{163}$Dy |
| | CD38 | CD38 | Immune | $^{142}$Nd |
| Misc | CDH | E-/P-cadherin | Epithelial | $^{173}$Yb |
| | CD31 | CD31 | Endothelial | $^{172}$Yb |
| | SMA | Smooth muscle actin | Stromal | $^{115}$In |
| | KI-67 | Ki-67 | Proliferating | $^{168}$Er |
| | pH3 | Phospho-histone H3 | Proliferating | $^{170}$Er |
| | pRB1 | Phospho-retinoblastoma | Cycling | $^{175}$Yb |
| | cPARP1 | Cleaved caspase 3 + poly (ADP-ribose) polymerase | Apoptotic | $^{176}$Yb |
| | CA9 | Carbonic anhydrase IX | Hypoxic | $^{166}$Er |
| | H3 | Histone H3 | Nuclei | $^{113}$In |
| | Ir191, Ir193 | (DNA intercalators) | DNA | $^{191}$Ir, $^{193}$Ir |

**Table 1. Imaging Mass Cytometry Panel**

# STAR METHODS

## CONTACT FOR REAGENT AND RESOURCE SHARING

Further information and requests for resources and reagents should be directed to and will be fulfilled by the Lead Contact, Bernd Bodenmiller (bernd.bodenmiller@imls.uzh.ch).

## EXPERIMENTAL MODEL AND SUBJECT DETAILS

### Human Organ Donors

Pancreas samples were obtained from nPOD (www.jdrfnpod.org). All procedures were approved by the University of Florida Institutional Review Board (IRB201600029) and the Zurich Cantonal Ethics Committee (2017-02302). Procedures were also approved by the United Network for Organ Sharing (UNOS) according to federal guidelines, and informed consent was obtained from each donor's legal representative. For each donor, a medical chart review was performed and C-peptide measured (Campbell-Thompson et al., 2012a) with T1D diagnosis determined or confirmed according to the ADA guidelines. Demographics, length of hospitalization, and organ transport duration information was obtained from hospital records or UNOS. Donor pancreata were recovered, shipped in transport media on ice via organ courier to the University of Florida, and processed by a licensed pathology assistant (Campbell-Thompson et al., 2012b). The cases were selected to represent recent onset T1D (< 0.5 years), long-standing T1D (≥ 8 years), and non-diabetes control. Four groups of three donors with different disease duration but matched by age and gender were analyzed. Additional donor information is listed in Table S1.

## METHOD DETAILS

### Antibody Testing and Validation

All antibodies in the panel (Table 1) were initially tested by IF on lymphoid tissues (spleen, tonsil, and lymph node) for antibodies targeting immune markers and on pancreas for the other markers.

Only antibodies that produced expression patterns consistent with the literature and a high signal intensity were conjugated to metals. After metal labeling, all antibodies were tested again by IMC to ensure that antibody specificity was not affected by conjugation. Finally, the entire antibody panel was used to stain two tissue arrays: an array containing large cores from six different tissues and a microarray containing 78 cores representing 20 different tissues from healthy subjects and cancer patients. In this way, each antibody could be positively validated on tissues known to express the target antigen and negatively validated on tissues known to be negative for that antigen. The main observations used to validate each antibody are listed in Table S2.

**Antibody Conjugation and Titration**

Antibodies were conjugated to metals using the MaxPar X8 Multimetal Labeling Kit (Fluidigm) according to the manufacturer's protocol. To determine optimal antibody concentrations, the antibody panel was divided in "odd" and "even" channels, depending on the atomic mass of the metal tag, and two-fold serial antibody dilutions were performed. Sections of human pancreas and lymphoid tissue (spleen, tonsil, pancreatic lymph node) were divided in four areas, and each area was stained with a different antibody dilution. Separate slides were used for antibodies conjugated to odd and even metal isotopes. After IMC measurement, each channel was examined visually and the dilution that produced the highest signal-to-noise ratio was selected. In the few cases where notable spillover was detected in the adjacent (+1 and -1) channels, a higher antibody dilution was selected.

**Tissue Staining**

Two sections per pancreas, from head, body, or tail, were stained with our full antibody panel (Table 1). Slides were incubated for 1 h at 60 °C in a dry oven, deparaffinized in fresh Xylol, and rehydrated through a graded alcohol series. Antigen retrieval was performed in a decloaking chamber (Medite) for 30 min at 96 °C in Tris-EDTA, pH 9.2. After blocking in buffer containing

10% normal horse serum, slides were incubated overnight at 4 °C with three primary antibodies: rabbit anti-glucagon-$^{156}$Gd, rabbit anti-synaptophysin-$^{160}$Gd, and goat anti-Pdx1 (unconjugated). The next day, slides were incubated with anti-rabbit IgG-Alexa Fluor 488 and anti-Goat IgG-$^{158}$Gd secondary antibodies for 1 h at room temperature, followed by Hoechst dye counterstaining (5 min at room temperature). Slide scanner imaging was performed at this stage (see *Selection of Areas of Interest* below). Two successive overnight incubations at 4 °C were then performed for labeling with the remainder of primary antibodies (13 primary antibodies on the first night and 19 on the second night). Finally, slides were counterstained with iridium intercalator for 5 min at room temperature, quickly dipped in doubly distilled $H_2O$, and immediately dried with pressurized air.

**Selection of Areas of Interest**

Pancreas sections stained for glucagon and synaptophysin and counterstained with Hoechst were imaged with a slide scanner (Zeiss Axio Scan.Z1) at 20X magnification. Areas of interest were chosen manually based on islet size (islets representing the complete spectrum of size observed but with an enrichment for large islets) and islet position (to ensure distribution of sampling over the whole section) (Figure S1A). Area size was defined as the axis-aligned minimum bounding box containing all islets in the area, expanded by 100 µm in all directions. The coordinates of areas of interest were recorded using ImageJ and transformed to IMC coordinates using a custom Python script (see Key Resources Table).

**IMC Image Acquisition**

Data acquisition was performed on a Helios time-of-flight mass cytometer (CyTOF) coupled to a Hyperion Imaging System (Fluidigm). Prior to laser ablation, optical images of slides were acquired using the Hyperion software, and the areas to ablate were selected as described above. Laser ablation was performed at a resolution of approximately 1 µm and a frequency of 200 Hz. Slides were acquired in a randomized order over 25 consecutive days. To ensure performance

stability, the machine was calibrated daily with a tuning slide spiked with five metal elements (Fluidigm). In total, 851 image stacks from 24 pancreas sections were acquired. Three were removed due to data corruption, one due to poor image quality, and two because the areas did not contain any islets. All analyses were performed on the 845 remaining image stacks.

## QUANTIFICATION AND STATISTICAL ANALYSIS

### IMC Data Preprocessing

Text format (.txt) files generated during data acquisition were converted to tiff images using a custom Python script (https://github.com/BodenmillerGroup/imctools). For visualization, false color images were prepared from tiff images using Fiji (https://fiji.sc).

### Spillover Compensation

Although spectral overlap between pure metal isotopes is very limited, channel crosstalk caused by isotopic impurity, oxide formation, and imprecision in ion detection still exist (Chevrier et al., 2018). To measure crosstalk from one channel to the other, we generated a slide spotted with the same metals used for antibody conjugation (one metal isotope per spot). With this strategy, each metal can be measured individually while having all channels open for detection, thus allowing for spillover quantification across all measured channels. The slide was measured three times during the 25 days of IMC data acquisition, and an average spillover matrix was generated from the resulting data (Figure S1B). This matrix was used to correct for spillover in our dataset (Figure S1C), as described (Chevrier et al., 2018).

### Image Segmentation

We generated cell segmentation masks in two steps: First, we used the interactive machine learning software ilastik to classify pixels as nucleus, cytoplasm/membrane, and background compartments. Second, we imported the probability maps generated by ilastik into CellProfiler to

identify individual nuclei, define cell borders, and generate cell masks. We adopted a similar approach to segment islets (Figure S3).

***Pixel Classification***

For cell segmentation, the pixels in each image were defined as belonging to the nucleus, cytoplasm, or background compartment using the pixel classification module of the open source software ilastik (Sommer et al., 2011) as described (Schulz et al., 2018) (https://github.com/BodenmillerGroup/ImcSegmentationPipeline). Training of the Random Forest classifier was performed on 125 x 125 pixels substacks generated from the original images and containing only informative markers (i.e., H3, CDH, CD99, CD44, MPO, SYP, KRT19, CD45, CD31, SMA, and Iridium). This allowed for the generation of maps that integrate for each pixel the probability of belonging to each of three compartments, as shown in Figure 1B (center). Based on the trained classifier, probability maps were generated for the whole dataset and exported as tiff files in batch mode.

***Cell Segmentation***

CellProfiler (Kamentsky et al., 2011) was subsequently used to define cell masks and quantify marker expression. To define cell borders, nuclei were first identified as primary objects based on ilastik probability maps and expanded through the cytoplasm compartment until either a neighboring cell or the background compartment was reached. Cell masks were generated for identification of single cells and used to extract single-cell information (marker abundance, spatial and neighborhood data) from the original images. The results were exported as csv tables for further analysis.

767

768 ***Islet and Blood Vessel Segmentation***

769 Islet and blood vessel segmentation was performed in a similar manner as cell segmentation with
770 the following modifications: *i)* for ilastik pixel classification, images were divided into islet, blood
771 vessels, and "other" (that is non-islet, non-vessel) compartments based on substacks containing
772 informative markers (i.e., SYP, CD99, CD31, CD45, AMY2A, KRT19, and Iridium); *ii)* in
773 CellProfiler, islets and blood vessels were directly defined as primary objects. Distance to islet rim
774 was measured by combining islet and cell masks, using a custom CellProfiler plugin
775 (https://github.com/BodenmillerGroup/ImcPluginsCP).

776

777 **Cell Type Definition**

778 The object classification module of ilastik was used to define cell types (Figure S3). First, binary
779 cell masks and substacks containing relevant markers (i.e., CD99, SYP, AMY2A, KRT19, CD44,
780 CDH, CD45, CD3, CD8, CD20, MPO, CD68, and SMA) were loaded into ilastik and a classifier
781 was trained in order to divide the cells in four main categories (islet, immune, exocrine, and
782 "other"). The resulting object predictions were exported as tiff images and imported into
783 CellProfiler to generate cell masks specific to each cell category. The process was iterated to
784 subdivide each category into cell types. For islet cell type definition, masks containing only cells
785 defined in the first step as belonging to the islet category were imported into ilastik, and a new
786 training was performed to attribute α, β, δ, and γ cell types based on the expression of islet-
787 expressed markers (i.e., INS, PIN, GCG, SST, PPY, PDX1, NKX6-1, IAPP, PCSK2, CD99, and
788 SYP). The same approach was adopted to define B cells, cytotoxic and helper T cells,
789 monocytes/macrophages, and neutrophils among immune cells (markers used: CD45, CD3e,
790 CD4, CD8a, CD20, CD68, MPO, and CD45RA). In addition, exocrine cells were divided into
791 acinar and ductal cells (markers used: KRT19, AMY2A, CD44, and CDH), and "other" cells were

792 divided into three cell types: endothelial (also includes peri-endothelial cells), stromal, and
793 unknown (markers used: SMA, CD31, CD68, and CDH).
794
795 **Pseudotime Analysis**
796 Pseudotime analysis was performed using the trajectory inference algorithm SCORPIUS
797 (Cannoodt et al., 2016), and results were confirmed using the Monocle2 DDRTree algorithm (Qiu
798 et al., 2017). Only islets containing 15 cells or more were considered. Islet expression profiles
799 and pseudotime ordering were based on the expression of islet-expressed markers averaged
800 over the islet sectional area. All measured islet markers were considered (INS, PIN, GCG, SST,
801 PDX1, NKX6-1, IAPP, PCSK2, SLC2A1, PTPRN, SYP, and CD99), except for PPY. The presence
802 of a γ cell-rich pancreas head section in one donor with long-duration T1D tended to confound
803 the algorithms, resulting in classification of the very few γ cell-rich islets from non-diabetic donors
804 into the long-duration (pseudostage 3) category. Raw IMC counts averaged over islet areas were
805 used as an input.
806
807 **Neighborhood Analysis**
808 Neighborhood analysis was performed using R and histoCAT (Schapiro et al., 2017). Custom
809 scripts were used to import cell type and pseudotime information into histoCAT (see Key
810 Resources Table). An expansion of 3 pixels was used to detect cell neighbors. The presence of
811 significant cell type association or avoidance was determined using 999 random permutations of
812 cell type labels and a significance threshold of $P < 0.01$. All other parameters and methods were
813 chosen as suggested in the original publication (Schapiro et al., 2017).
814
815 **Data Analysis**
816 Data were analyzed and graphed using R and histoCAT (Schapiro et al., 2017). In particular, an
817 R implementation of tSNE (https://cran.r-project.org/web/packages/tsne) was used to generate

tSNE maps (van der Maaten and Hinton, 2008). Unless otherwise stated, raw IMC counts were 99$^{th}$-percentile-normalized and scaled from 0 to 1 (scaled counts).

**Statistics**

Statistical tests were performed using R. Statistical parameters are reported in the figure legends. For pairwise group comparisons, we systematically used a non-parametric statistical test (unpaired, two-tailed Mann-Whitney *U* test) and applied the Holm post-hoc adjustment method to correct for multiple comparisons. Overall, the *P* value significance threshold was defined as 0.01. In text and figures, *N* represents the number of donors and *n* represents either the number of cells or the number of islets (as indicated in figure legends). In histograms, bars represent the means and error bars represent standard errors of the mean. Correlation analyses in Figure 4H were performed using Pearson's *r* correlation coefficient. As mentioned above (see the IMC Image Acquisition paragraph), six out of 851 IMC images were excluded because of data corruption, poor image quality, or absence of islets. No other data or values were excluded from our analyses.

**DATA AND SOFTWARE ABILITY**

Raw IMC data (including image stacks, single-cell data and islet-level data) are available from Mendeley Data (http://dx.doi.org/10.17632/cydmwsfztj.1). Custom code generated by the Bodenmiller lab for IMC data preprocessing and image segmentation is available online (https://github.com/BodenmillerGroup); histoCAT can be downloaded as a standalone application from the project page (https://github.com/BodenmillerGroup/histoCAT). Scripts for IF-to-IMC coordinate transformation, as well as code related to neighborhood analysis (cell type and pseudotime import and custom clustering) are available from Mendeley data (http://dx.doi.org/10.17632/cydmwsfztj.1).

Figure 1

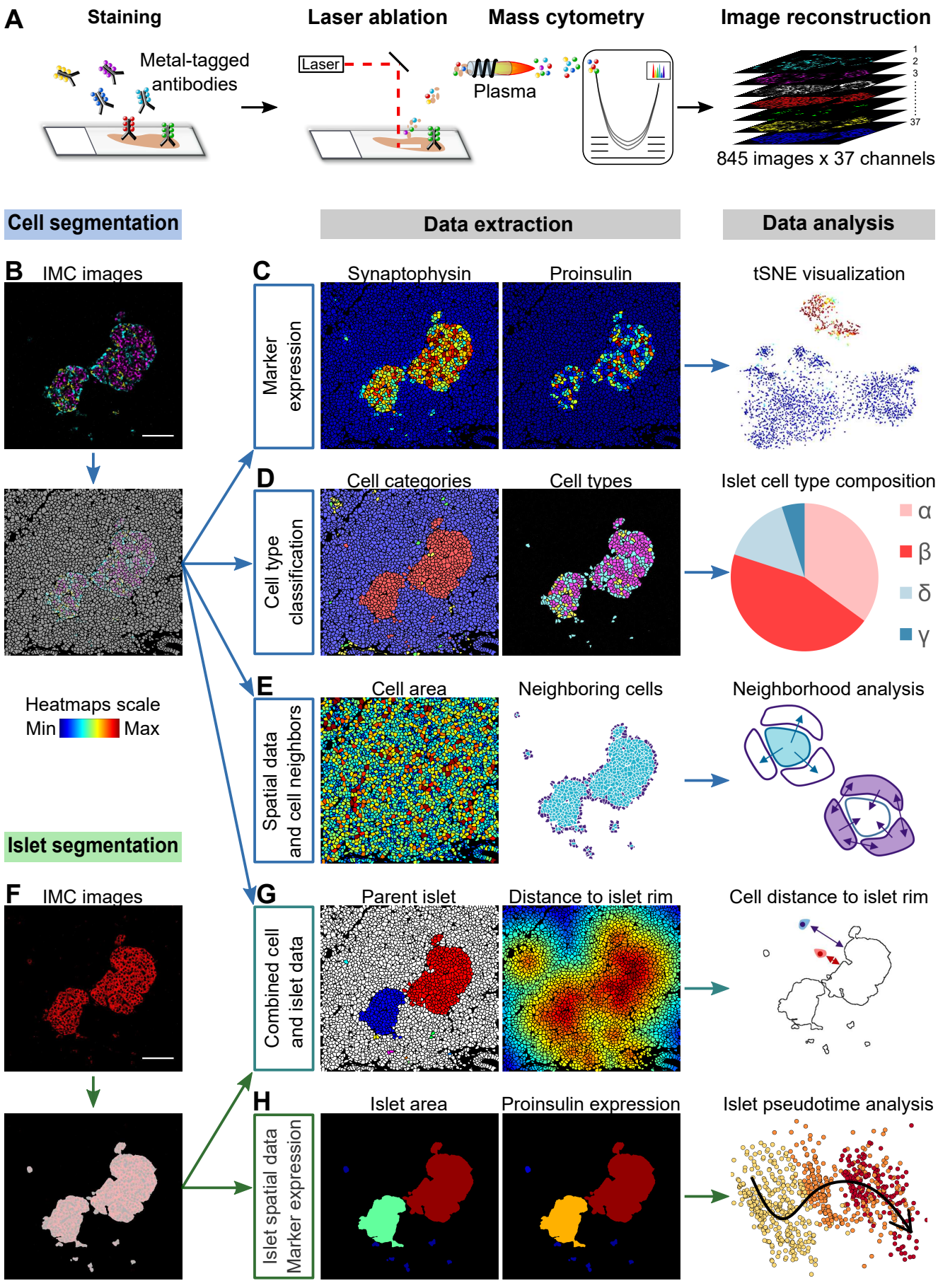
A
Staining
Laser ablation
Mass cytometry
Image reconstruction
Metal-tagged antibodies
Laser
Plasma
845 images x 37 channels
Cell segmentation
Data extraction
Data analysis
B IMC images
C
Synaptophysin
Proinsulin
tSNE visualization
Marker expression
D
Cell categories
Cell types
Islet cell type composition
Cell type classification
α
β
δ
γ
E
Cell area
Neighboring cells
Neighborhood analysis
Spatial data and cell neighbors
Heatmaps scale
Min
Max
Islet segmentation
F IMC images
G
Parent islet
Distance to islet rim
Cell distance to islet rim
Combined cell and islet data
H
Islet area
Proinsulin expression
Islet pseudotime analysis
Islet spatial data Marker expression

Figure 2

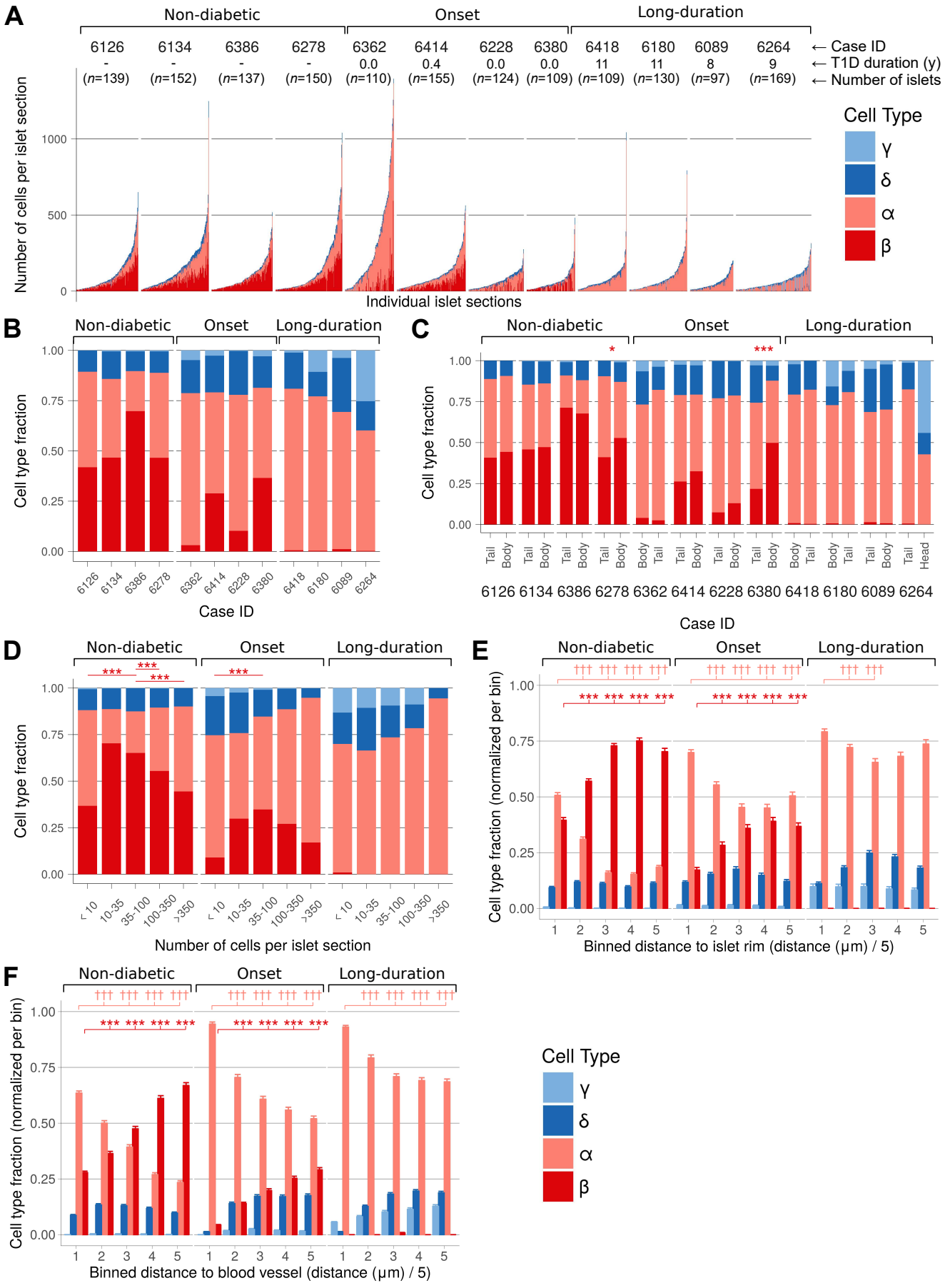
A
Non-diabetic
Onset
Long-duration
6126 - (n=139)
6134 - (n=152)
6386 - (n=137)
6278 - (n=150)
6362 0.0 (n=110)
6414 0.4 (n=155)
6228 0.0 (n=124)
6380 0.0 (n=109)
6418 11 (n=109)
6180 11 (n=130)
6089 8 (n=97)
6264 9 (n=169)
← Case ID
← T1D duration (y)
← Number of islets
Number of cells per islet section
Individual islet sections
Cell Type
γ
δ
α
β
B
Cell type fraction
Case ID
C
Cell type fraction
Tail
Body
Head
6126 6134 6386 6278 6362 6414 6228 6380 6418 6180 6089 6264
D
Cell type fraction
Number of cells per islet section
E
Cell type fraction (normalized per bin)
Binned distance to islet rim (distance (µm) / 5)
F
Cell type fraction (normalized per bin)
Binned distance to blood vessel (distance (µm) / 5)
Cell Type
γ
δ
α
β

Figure 3

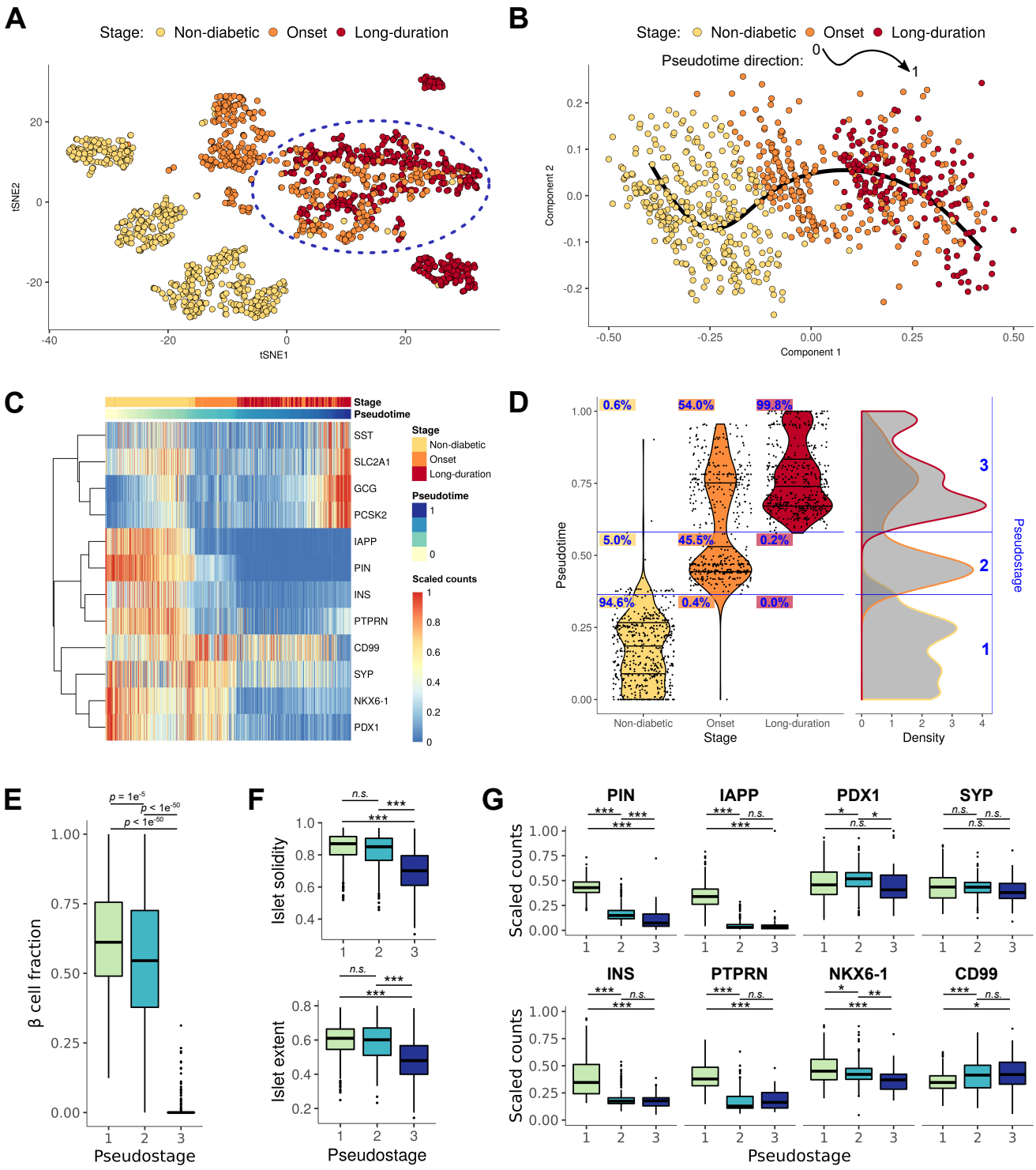
A
Stage: Non-diabetic Onset Long-duration
tSNE2
tSNE1
B
Stage: Non-diabetic Onset Long-duration
Pseudotime direction: 0 1
Component 2
Component 1
C
Stage
Pseudotime
SST
SLC2A1
GCG
PCSK2
IAPP
PIN
INS
PTPRN
CD99
SYP
NKX6-1
PDX1
Stage
Non-diabetic
Onset
Long-duration
Pseudotime
Scaled counts
D
0.6%
54.0%
99.8%
5.0%
45.5%
0.2%
94.6%
0.4%
0.0%
Pseudotime
Non-diabetic
Onset
Long-duration
Stage
Density
Pseudostage
E
p = 1e-5
p < 1e-50
p < 1e-50
β cell fraction
Pseudostage
F
Islet solidity
Islet extent
Pseudostage
G
PIN
IAPP
PDX1
SYP
INS
PTPRN
NKX6-1
CD99
Scaled counts
Pseudostage

Figure 4

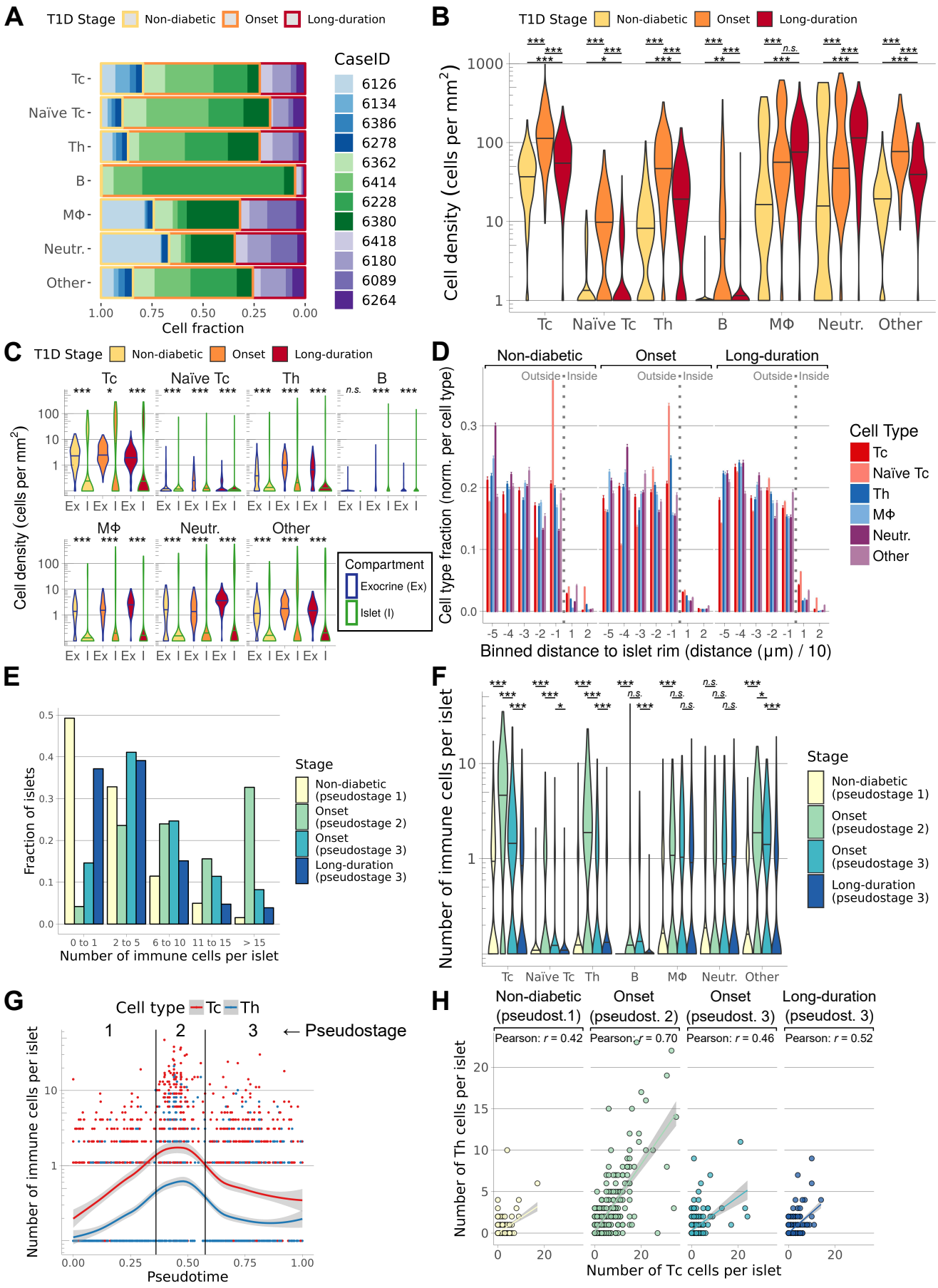
A
T1D Stage
Non-diabetic
Onset
Long-duration
CaseID
6126
6134
6386
6278
6362
6414
6228
6380
6418
6180
6089
6264
Tc
Naïve Tc
Th
B
MΦ
Neutr.
Other
Cell fraction
B
Cell density (cells per mm2)
C
Compartment
Exocrine (Ex)
Islet (I)
D
Non-diabetic
Onset
Long-duration
Outside
Inside
Cell type fraction (norm. per cell type)
Binned distance to islet rim (distance (µm) / 10)
Cell Type
E
Fraction of islets
Number of immune cells per islet
Stage
Non-diabetic (pseudostage 1)
Onset (pseudostage 2)
Onset (pseudostage 3)
Long-duration (pseudostage 3)
F
Number of immune cells per islet
G
Cell type
Tc
Th
← Pseudostage
Pseudotime
H
Pearson: r = 0.42
Pearson: r = 0.70
Pearson: r = 0.46
Pearson: r = 0.52
Number of Th cells per islet
Number of Tc cells per islet

Figure 5

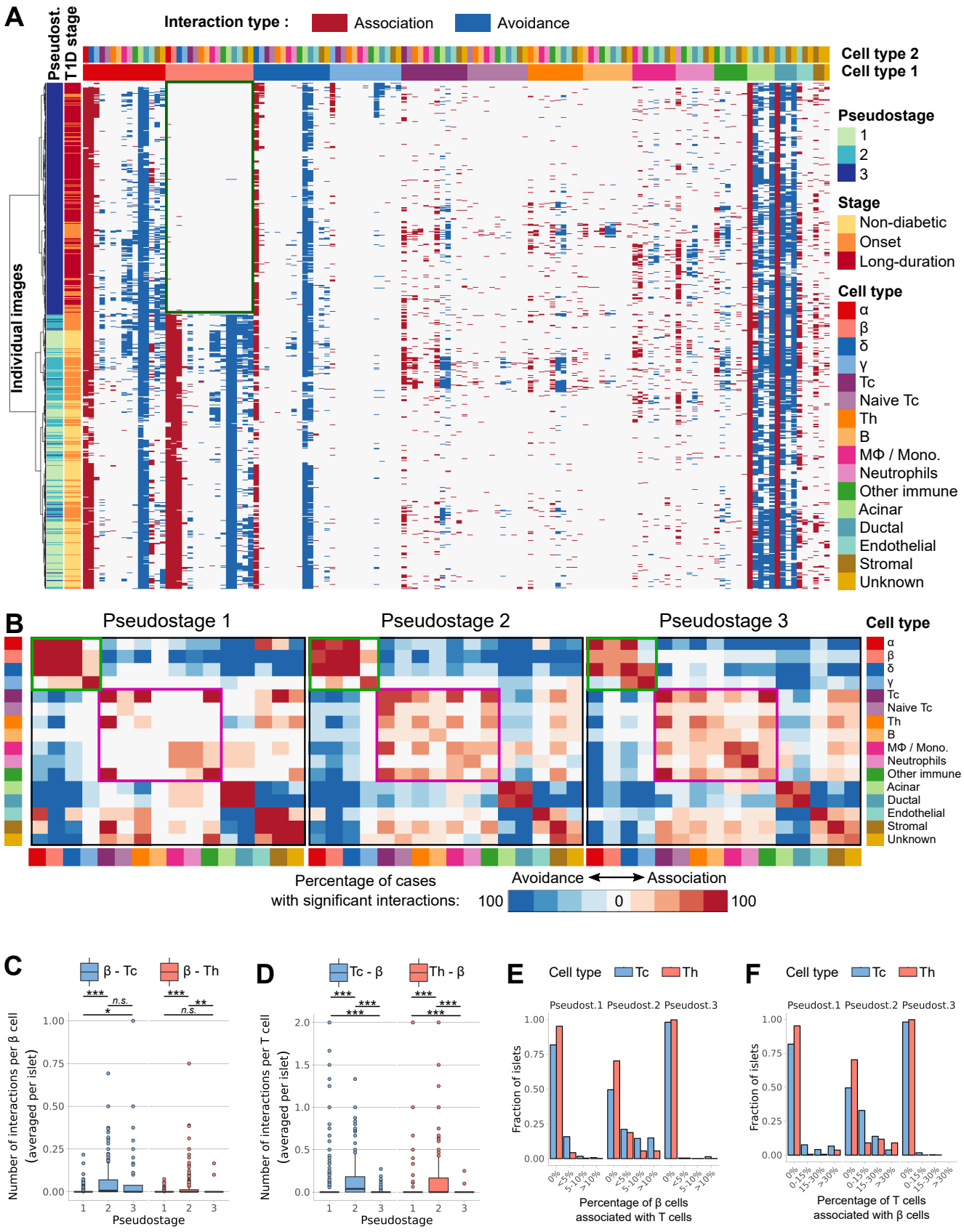
A
Interaction type :
Association
Avoidance
Pseudost.
T1D stage
Individual images
Cell type 2
Cell type 1
Pseudostage
1
2
3
Stage
Non-diabetic
Onset
Long-duration
Cell type
α
β
δ
γ
Tc
Naive Tc
Th
B
MΦ / Mono.
Neutrophils
Other immune
Acinar
Ductal
Endothelial
Stromal
Unknown
B
Pseudostage 1
Pseudostage 2
Pseudostage 3
Cell type
Percentage of cases
with significant interactions:
Avoidance
Association
100
0
100
C
β - Tc
β - Th
Number of interactions per β cell
(averaged per islet)
Pseudostage
D
Tc - β
Th - β
Number of interactions per T cell
(averaged per islet)
Pseudostage
E
Cell type
Tc
Th
Pseudost.1
Pseudost.2
Pseudost.3
Fraction of islets
Percentage of β cells
associated with T cells
F
Cell type
Tc
Th
Pseudost.1
Pseudost.2
Pseudost.3
Fraction of islets
Percentage of T cells
associated with β cells

## KEY RESOURCES TABLE

| REAGENT or RESOURCE | SOURCE | IDENTIFIER |
|---|---|---|
| **Antibodies** | | |
| Mouse monoclonal anti-Alpha smooth muscle actin | Abcam | Cat#ab76549, RRID:AB_2223019 |
| Goat polyclonal anti-Carbonic anhydrase IX | R and D Systems | Cat#AF2188, RRID:AB_416562 |
| Rabbit monoclonal anti-Caspase 3 | BD Biosciences | Cat#559565, RRID:AB_397274 |
| Rabbit monoclonal anti-CD3ε | Cell Signaling Technology | Cat#85061, RRID:AB_2721019 |
| Goat polyclonal anti-CD4 | R and D Systems | Cat#AF-379-NA, RRID:AB_354469 |
| Mouse monoclonal anti-CD8a | Thermo Fisher Scientific | Cat#14-0085-82, RRID:AB_11150240 |
| Mouse monoclonal anti-CD20 | Thermo Fisher Scientific | Cat#14-0202-82, RRID:AB_10734340 |
| Mouse monoclonal anti-CD31 | Novus | Cat#NB600-562, RRID:AB_10002476 |
| Rabbit monoclonal anti-CD38 | Abcam | Cat#ab108403; RRID: AB_10890803 |
| Rat monoclonal anti-CD44 | BD Biosciences | Cat#550538, RRID:AB_393732 |
| Mouse monoclonal anti-CD45 | Thermo Fisher Scientific | Cat#14-9457-82, RRID:AB_11063696 |
| Mouse monoclonal anti-CD45RA | BioLegend | Cat#304102, RRID:AB_314406 |
| Mouse monoclonal anti-CD68 | Thermo Fisher Scientific | Cat#14-0688-82, RRID:AB_11151139 |
| Mouse monoclonal anti-CD99 | BioLegend | Cat#318002, RRID:AB_604112 |
| Mouse monoclonal anti-E-Cadherin | BD Biosciences | Cat#610182, RRID:AB_397581 |
| Rabbit monoclonal anti-Keratin 19 | Cell Signaling Technology | Cat#13092, RRID:AB_2722626 |
| Mouse monoclonal anti-Foxp3 | Thermo Fisher Scientific | Cat#14-4777-80, RRID:AB_467555 |
| Rabbit monoclonal anti-Glucagon | Cell Signaling Technology | Cat#8233, RRID:AB_10859908 |
| Rabbit monoclonal anti-Glucose Transporter 1 | Abcam | Cat#ab115730, RRID:AB_10903230 |
| Donkey polyclonal anti-Goat IgG | Thermo Fisher Scientific | Cat#PA1-28659, RRID:AB_10981355 |
| Rabbit monoclonal anti-Histone H3 | Cell Signaling Technology | Cat#4499, RRID:AB_10544537 |
| Rat monoclonal anti-Histone H3 Phospho (Ser28) | BioLegend | Cat#641002, RRID:AB_1227659 |
| Rabbit monoclonal anti-Insulin | Cell Signaling Technology | Cat#3014, RRID:AB_2126503) |
| Rabbit polyclonal anti-IAPP | Atlas Antibodies | Cat#HPA053194, RRID:AB_2682076 |
| Mouse monoclonal anti-Ki-67 | BD Biosciences | Cat#556003, RRID:AB_396287 |
| Rabbit polyclonal anti-Myeloperoxidase | Dako | Cat#A0398, RRID:AB_2335676 |
| Rabbit monoclonal anti-Nkx6.1 | Cell Signaling Technology | Cat#54551, RRID:AB_2722625 |
| Rabbit polyclonal anti-Pancreatic Amylase | Abcam | Cat#ab21156, RRID:AB_446061 |
| Mouse-monoclonal anti-Pancreatic Polypeptide | R and D Systems | Cat#MAB62971, RRID:AB_11127208 |
| Mouse monoclonal anti-cleaved PARP (Poly [ADP-Ribose] Polymerase) | BD Biosciences | Cat#552597, RRID:AB_394438 |
| Goat polyclonal anti Pdx1 | R and D Systems | Cat#AF2419, RRID:AB_355257 |
| Mouse monoclonal anti-Proinsulin | Abcam | Cat#ab8301, RRID:AB_306453 |
| Rabbit polyclonal anti-Prohormone Convertase 2 | Merck | Cat#AB15601-I, RRID:AB_2722624 |
| Rabbit polyclonal anti-PTPRN | Sigma-Aldrich | Cat#HPA007179, RRID:AB_1079714 |
| Rabbit polyclonal anti-phospho Rb (Ser807/811) | Cell Signaling Technology | Cat#9308, RRID:AB_331472 |
| Rabbit polyclonal anti-Somatostatin | Dako | Cat#A0566, RRID:AB_10013726 |
| Rabbit monoclonal Synaptophysin | Abcam | Cat#ab32127, RRID:AB_2286949 |

| | | |
|---|---|---|
| Donkey polyclonal anti-rabbit IgG, Alexa Fluor 488 | Thermo Fisher Scientific | Cat#A-21206, RRID:AB_2535792 |
| **Biological Samples** | | |
| Human pancreas sections | nPOD, University of Florida, Gainesville, FL 32610-0275 | https://www.jdrfnpod.org |
| **Chemicals, Peptides, and Recombinant Proteins** | | |
| Hoechst | Sigma Aldrich | Cat #94403-1ML |
| Iridium intercalator | Fluidigm | Cat #201192B |
| **Critical Commercial Assays** | | |
| MaxPar X8 Multimetal Labeling Kit | Fluidigm | Cat# 201300 |
| **Deposited Data** | | |
| IMC images | This paper | http://dx.doi.org/10.17632/cydmwsfztj.1 |
| **Software and Algorithms** | | |
| CellProfiler 2.2.0 | (Kamentsky et al., 2011) | http://cellprofiler.org |
| Fiji (ImageJ 1.51u) | (Schindelin et al., 2012) | https://fiji.sc |
| histoCAT 1.73 | (Schapiro et al., 2017) | https://github.com/BodenmillerGroup/histoCAT/releases |
| Ilastik 1.2.2 | (Sommer et al., 2011) | http://ilastik.org |
| Python 3.4.3 | Python Software Foundation | https://www.python.org |
| R 3.4.1 | R Development Core Team | https://www.r-project.org |
| Tools for IMC data processing | Bodenmiller lab | https://github.com/BodenmillerGroup/imctools |
| IMC data segmentation pipeline | Bodenmiller lab | https://github.com/BodenmillerGroup/ImcSegmentationPipeline |
| Custom CellProfiler plugins | Bodenmiller lab | https://github.com/BodenmillerGroup/ImcPluginsCP |
| Code and guidelines for spillover compensation | Bodenmiller lab | https://github.com/BodenmillerGroup/cyTOFcompensation |
| IF-to-IMC coordinate transformation | This paper | http://dx.doi.org/10.17632/cydmwsfztj.1 |
| Code related to neighborhood analysis | This paper | http://dx.doi.org/10.17632/cydmwsfztj.1 |
| SCORPIUS 1.0 | (Cannoodt et al., 2016) | https://github.com/rcannood/SCORPIUS |
| Monocle2 | (Qiu et al., 2017) | http://cole-trapnell-lab.github.io/monocle-release/docs |
| R implementation of tSNE | Justin Donaldson | https://cran.r-project.org/web/packages/tsne |

# INVENTORY OF SUPPLEMENTAL INFORMATION

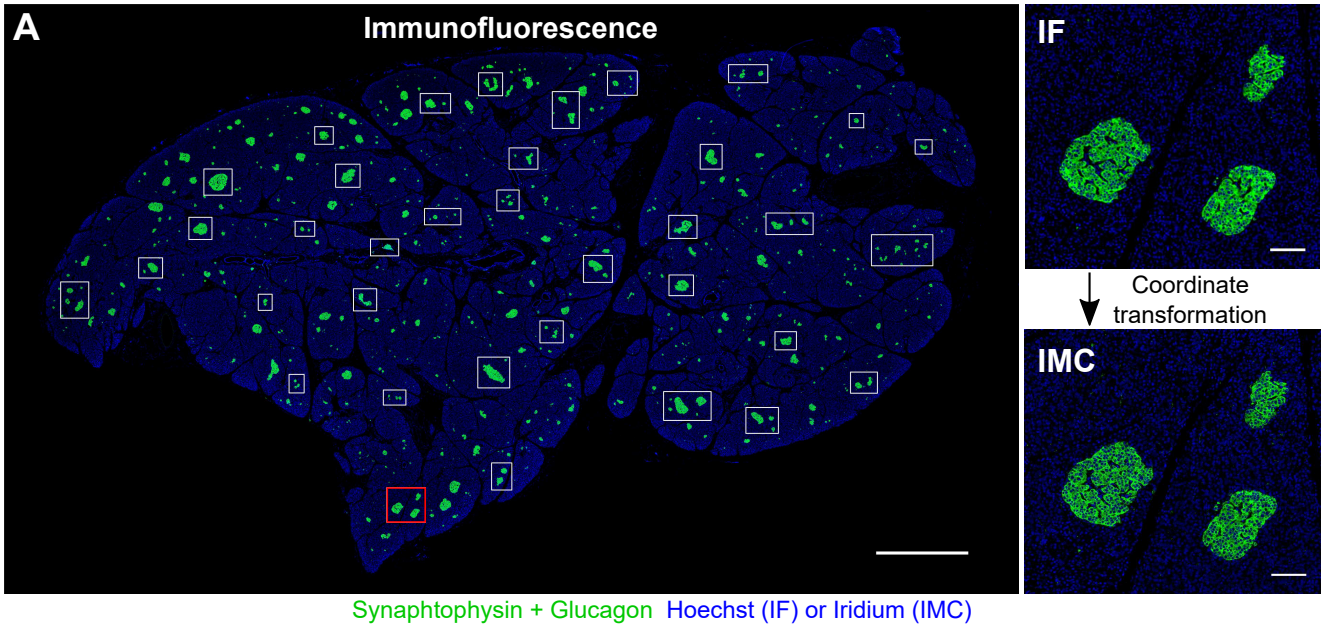


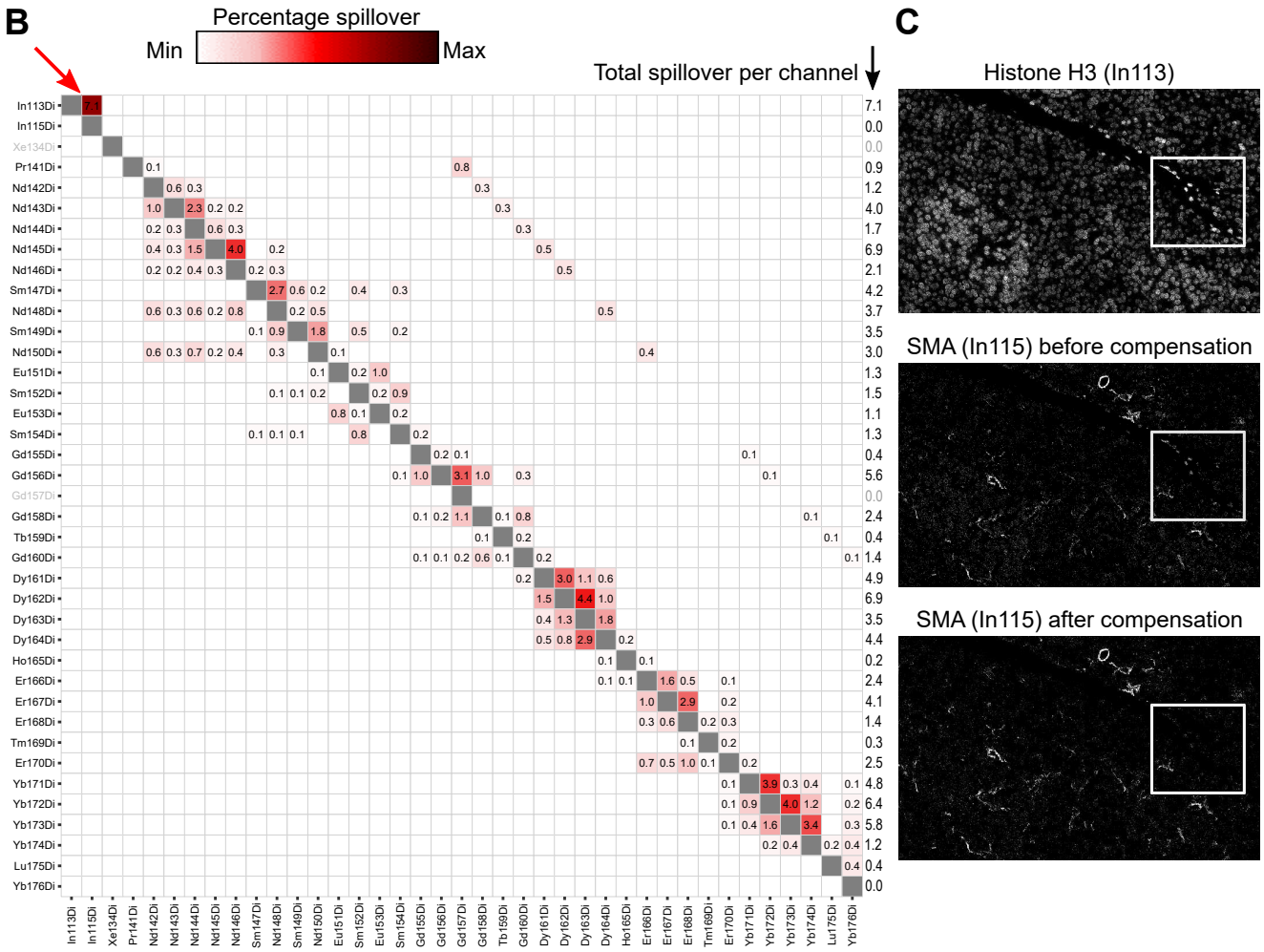


**Figure S1. Selection of Areas of Interest and Spillover Compensation**

*(legend on next page)*

**Figure S1. Selection of Areas of Interest and Spillover Compensation. Related to STAR Methods**

**A.** Slide-scanner immunofluorescence (IF) image of a pancreas section (tail from nPOD case 6278) stained for synaptophysin and glucagon (green) and counterstained with Hoechst (blue). White boxes indicate areas selected for analysis by IMC. The area indicated by a red box is shown at higher magnification on the right (top) and the same area imaged by IMC is shown below (bottom right). Channels shown on the IMC picture are glucagon plus synaptophysin (green) and iridium (Ir193, blue). Scale bars, 2000 μm (left), 100 μm (right).

**B.** Spillover matrix generated from single isotope measurements. Values represent the percentage of signal from the row channels observed in the column channels. The red arrow indicates spillover from channel $^{113}$In into channel $^{115}$In.

**C.** Images illustrating compensation of spillover from channel $^{113}$In into channel $^{115}$In. The white boxes highlight bright nuclei observed in the Histone H3 channel (top). The signal spills into the SMA channel (middle). After compensation, the spillover is removed from the SMA channel (bottom).

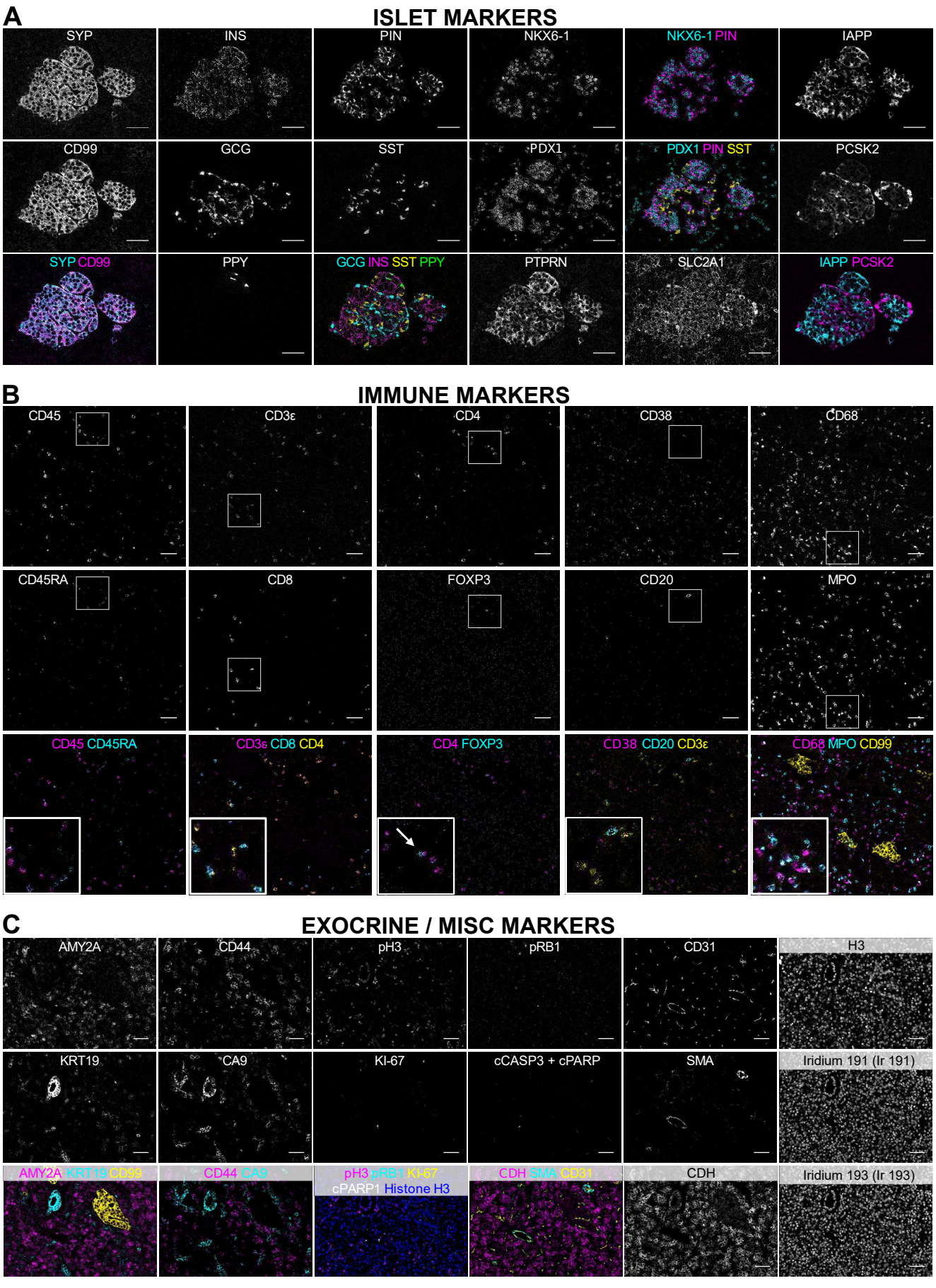


**Figure S2. Human Pancreas Imaging by IMC** *(legend on next page)*

**Figure S2. Human Pancreas Imaging by IMC. Related to Figure 1**

**A.** Representative images of the islet markers in our dataset. Relevant marker combinations are shown in color. Images are from a non-diabetic donor (nPOD case 6134).

**B.** Representative images of the immune markers in our dataset (grayscale images). Relevant marker combinations are shown in color. Images are from a donor with recent-onset T1D (nPOD case 6380). Insets show higher magnification of the white boxes indicated in individual marker images. The white arrow indicates a CD4+FOXP3+ cell.

**C.** Representative images of the other markers in our dataset (grayscale images). Relevant marker combinations are shown in color. Images are from a non-diabetic donor (nPOD case 6126).

Scale bars: 50 μm.

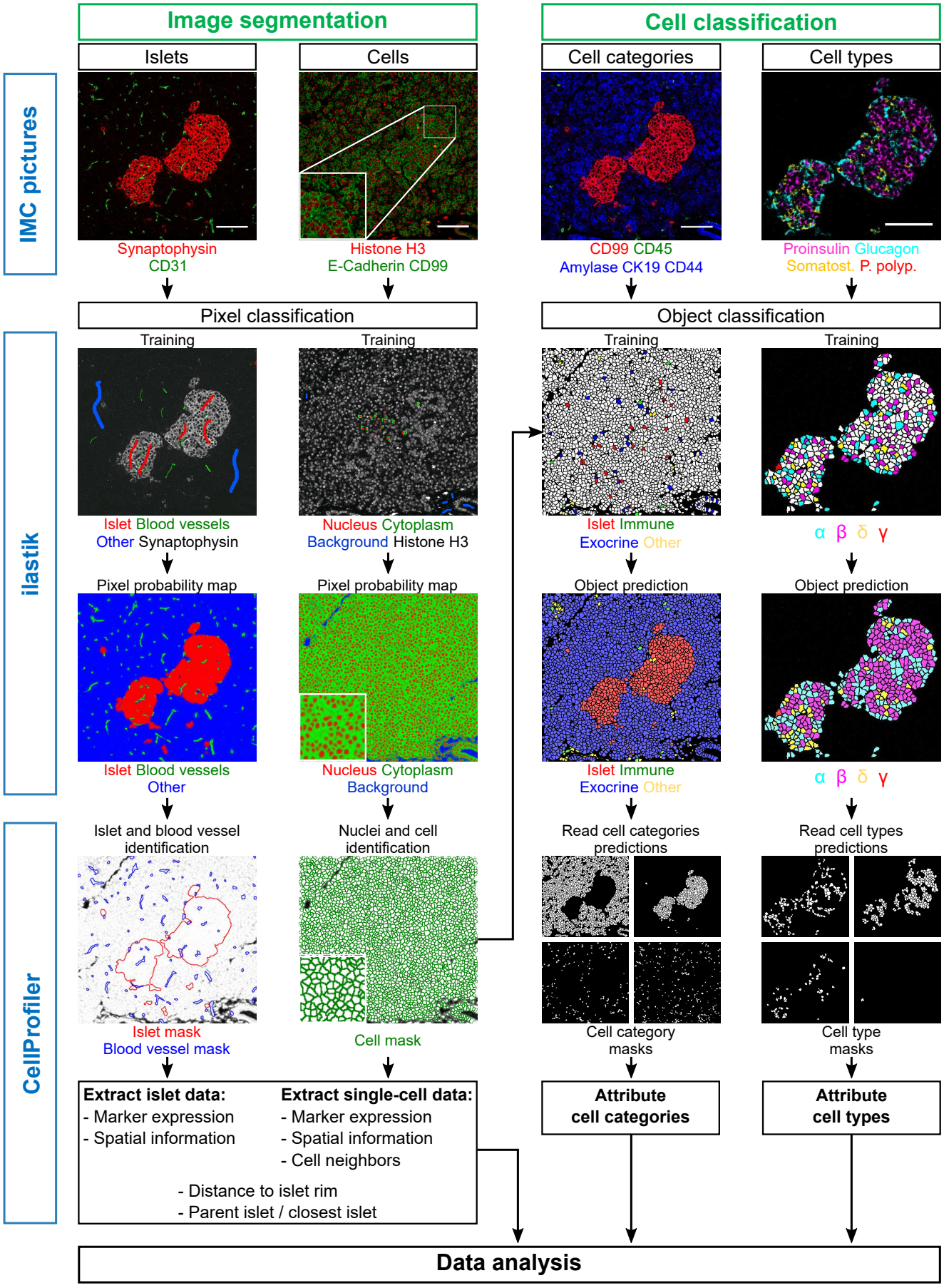


**Figure S3. Pipeline for IMC Data Processing**

*(legend on next page)*

**Figure S3. Pipeline for IMC Data Processing. Related to STAR Methods**

Based on the expression of relevant markers, IMC images are segmented into individual islets and cells (left). For islet segmentation, a Random Forest classifier is trained in ilastik, and each pixel is attributed to the islet (red), blood vessel (green), or "other" (blue) compartment. This yields a probability map that allows generation of islet and blood vessel masks in CellProfiler, which are then used to extract islet-level data. For cell segmentation, each pixel is classified into the nucleus (red), cytoplasm/membrane (green), or background (blue) compartment in ilastik. CellProfiler first identifies individual nuclei from ilastik probability maps and then expands these nuclei to find cell borders. Finally, cell masks are used to extract cell-level information and are combined with islet masks to extract additional spatial information (e.g., distance to islet rim). Attribution of cell types to all segmented cells is performed in two steps. First, cells are classified into four categories in ilastik (islet, immune, exocrine, other) based on the expression of relevant markers. The resulting prediction masks are then used to perform cell type attribution within each cell category. For instance, cells belonging to the "islet" category are attributed to the α, β, δ, or γ cell type (right). Immune cell types are defined in the same fashion and cell types are extracted from ilastik predictions using CellProfiler. Insets in the second column show higher magnification. Scale bars: 100 μm.

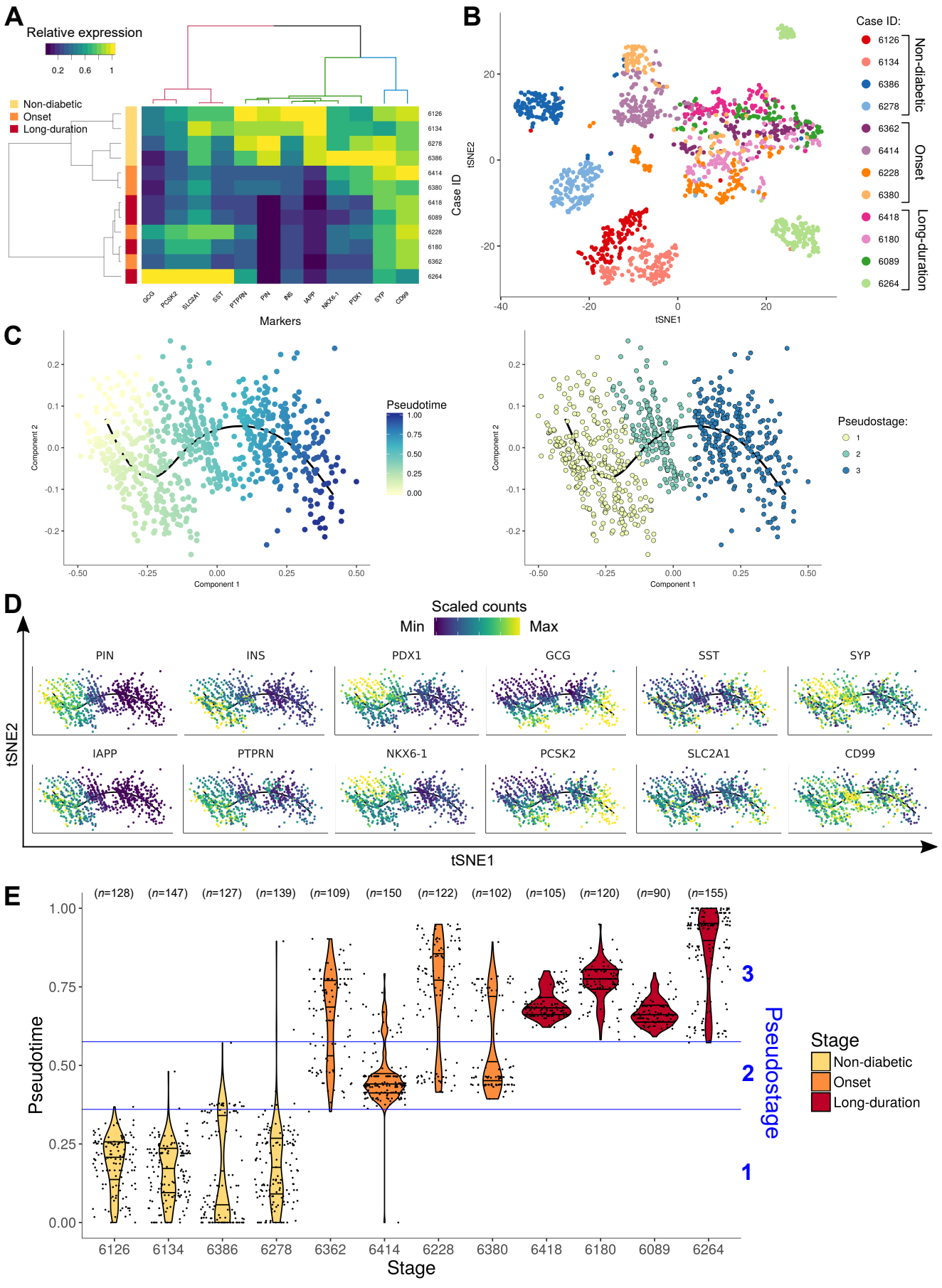


**Figure S4. Islet-Level Analysis**

*(legend on next page)*

**Figure S4. Islet-Level Analysis. Related to Figure 3.**

**A.** Hierarchical clustering of pancreas donors based on the expression of islet markers measured at the islet level (protein abundance averaged over the islet surface). The disease stage of each donor is color-coded on the left. *n* = 1494 islets (90 to 155 per donor).

**B.** tSNE visualization of islets, as in Figure 3A, color-coded by donor (nPOD case IDs and T1D stages are indicated on the right).

**C.** Islet pseudotime (left) and pseudostages (right) overlaid on the SCORPIUS map. *n* = 1494 islets (90 to 155 per donor).

**D.** Evolution of islet markers expression levels through pseudotime progression overlaid on the SCORPIUS map.

**E.** Violin plots showing pseudotime distribution for individual donors (one dot = one islet, the number of islets per donor, *n*, is indicated on top of the plot). Pseudostages, as defined in Figure 3D, are indicated in blue and pseudostage separation is indicated by horizontal blue lines.

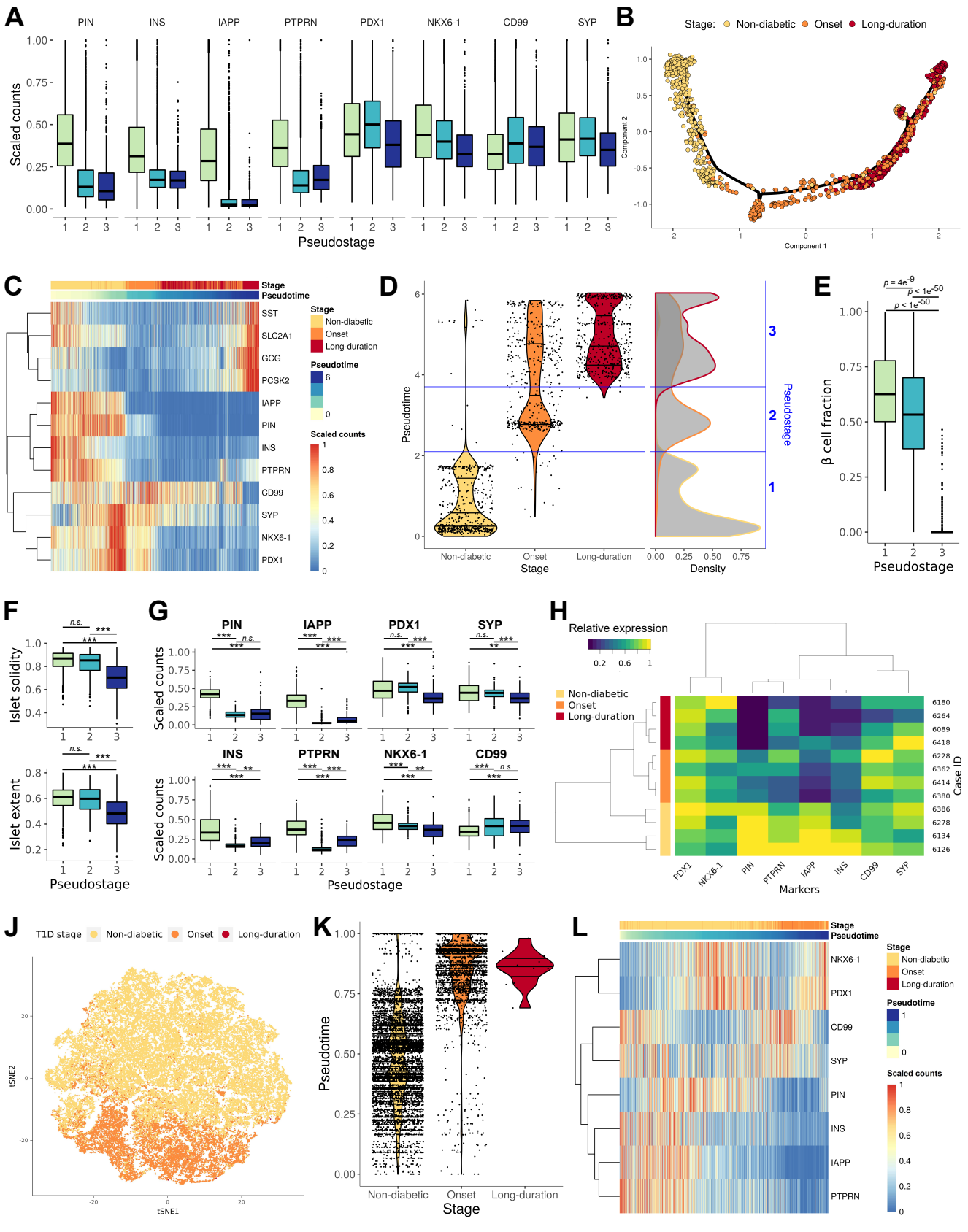


**Figure S5. Islet and β Cell Pseudotime Analysis**

*(legend on next page)*

**Figure S5. Islet and β Cell Pseudotime Analysis. Related to Figure 3**

**A.** Evolution of β cell marker expression in individual β cells through pseudostages. Same data as in Figure 3G shown at the β cell level to visualize β cell heterogeneity. Number of β cells analyzed: pseudostage 1, $n$ = 38,479 β cells; pseudostage 2, $n$ = 16,103 β cells; pseudostage 3, $n$ = 618 β cells.

**B.** Pseudotime analysis of islet expression profiles using Monocle2. Ordering was performed based on the expression of islet markers (one dot = one islet, $n$ = 1494 islets). The black line represents the trajectory computed by Monocle2.

**C.** Heatmap showing the expression levels of islet markers. Columns represent individual islets arranged according to pseudotime progression (computed with Monocle2). Horizontal bars on top indicate donor stage and islet pseudotime.

**D.** Violin plots showing islet distribution over pseudotime for controls and donors with T1D (left). Pseudostage separations are based on the density distribution of islets over Moncole2-computed pseudotime (right) and are indicated by horizontal blue lines. Pseudostages are indicated in blue.

**E.** Islet β cell fraction, as measured for the three Monocle2-defined pseudostages.

**F.** Islet extent and solidity measured for each Monocle2-defined pseudostage. Pairwise comparisons of the three pseudostages: *, $P < 0.01$; **, $P < 0.001$; ***, $P < 0.0001$, *n.s.*, not significant (Mann-Whitney $U$ test with Holm adjustment).

**G.** Evolution of β cell markers expression in β cells through Monocle2-defined pseudostages. Expression levels were measured in individual β cells and averaged for each islet. Pairwise comparisons of the three pseudostages: *, $P < 0.01$; **, $P < 0.001$; ***, $P < 0.0001$, *n.s.*, not significant (Mann-Whitney $U$ test with Holm adjustment).

**H.** Hierarchical clustering of pancreas donors based on the expression of islet markers measured at the β cell level. The disease stage of each donor is color-coded on the left and nPOD case IDs are indicated on the right.

**J.** tSNE map representing the expression profiles of β cells from 12 donors at different stages of T1D (one dot = one β cell).

**K.** Violin plots showing β cell distribution over SCORPIUS-computed pseudotime for the three disease stages. Dots represent individual β cells.

**L.** Heatmap showing expression of β cell markers with columns representing β cells arranged according to pseudotime progression. Horizontal bars on the top of the heatmap indicate donor disease stage and pseudotime.

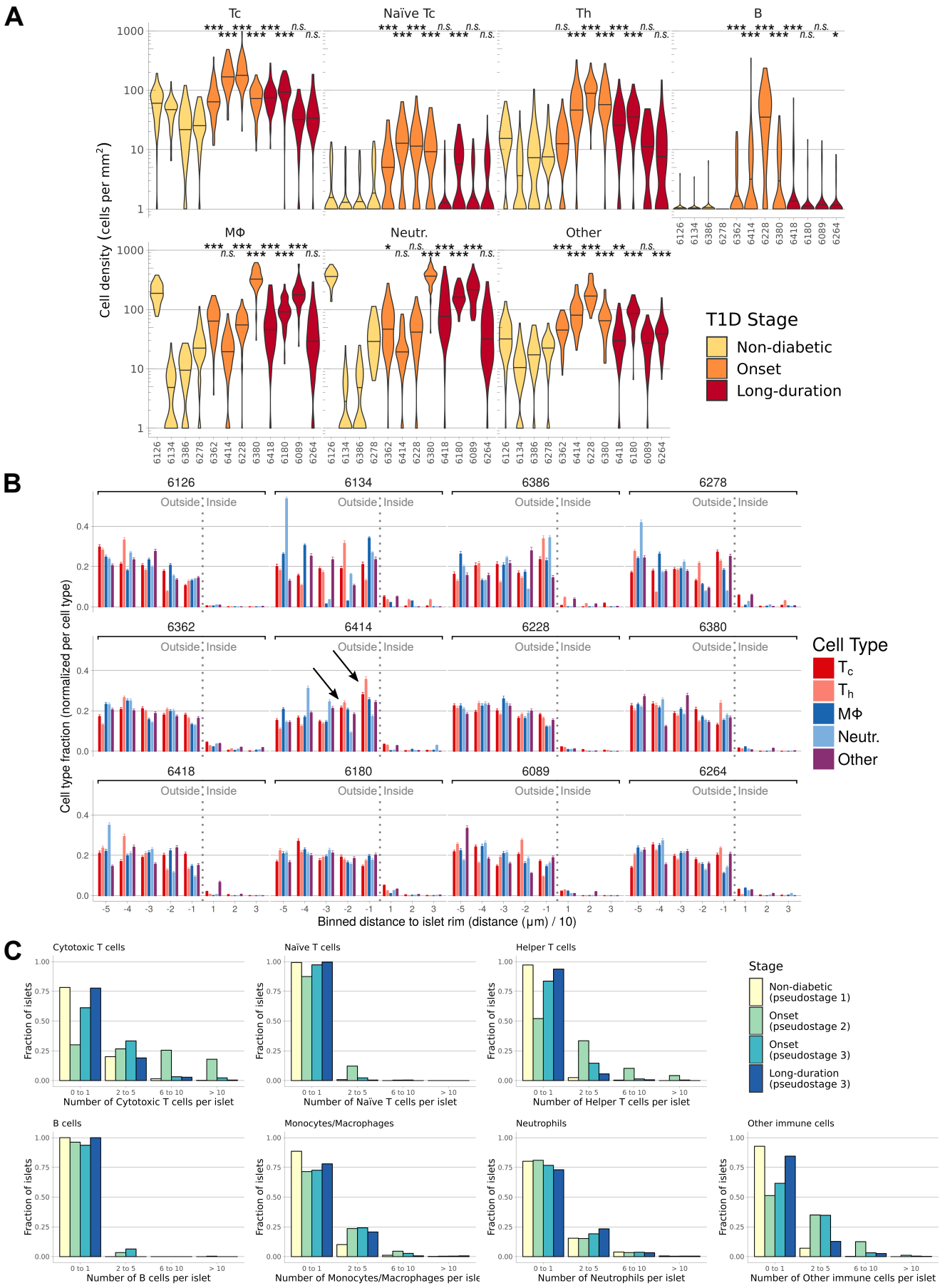


**Figure S6. Distribution of Immune Cell Types per Donor** *(legend on next page)*

**Figure S6. Distribution of Immune Cell Types per Donor. Related to Figure 4**

**A.** Density of immune cell types over IMC images measured for each donor. For each cell type, cell densities for individual donors with T1D were compared to the average value for non-diabetic donors (Mann-Whitney *U* test with Holm adjustment; *, $P < 0.01$; **, $P < 0.001$; ***, $P < 0.0001$; *n.s.*, not significant).

**B.** Average number of immune cells over binned distance to islet rim measured for each donor. Cell fractions are normalized by cell type. One bin corresponds to a distance of 10 µm with negative and positive values representing bins located outside and inside islets, respectively. The dotted vertical lines indicate the islet rim. Arrows indicate increased Tc and Th cell numbers around islets from nPOD case 6414. B cells and naïve Tc cells were not numerous enough to be meaningfully plotted. Error bars, SEM.

**C.** Fraction of islets containing given numbers of associated immune cells (inside the islet or within 20 µm of the islet rim), for all analyzed cell types, in function of the disease stage and pseudostage.

**Table S1. Human Donors: Clinical Data. Related to STAR Methods**

| nPOD case ID | Group for data analysis | Imaged pancreas regions | Matched group | Age (years) | Gender | Race | BMI | Donor type | Diabetes duration (years) |
|---|---|---|---|---|---|---|---|---|---|
| **6126** | Non-diabetic | Tail Body | 1 | 25.2 | Male | Caucasian | 25.1 | Non-diabetic | - |
| **6134** | Non-diabetic | Tail Body | 2 | 26.7 | Male | Caucasian | 20.1 | Non-diabetic | - |
| **6386** | Non-diabetic | Tail Body | 3 | 14 | Male | Caucasian | 23.9 | Non-diabetic | - |
| **6278** | Non-diabetic | Tail Body | 4 | 12 | Female | African-American | 21.3 | Non-diabetic | - |
| **6362** | Onset | Tail Body | 1 | 24.9 | Male | Caucasian | 28.5 | T1D | 0.0 (7.75 days) |
| **6414** | Onset | Tail Body | 2 | 23.1 | Male | African-American | 24.3 | T1D | 0.4 |
| **6228** | Onset | Tail Body | 3 | 13.0 | Male | Caucasian | 17.4 | T1D | 0.0 (9.5 days) |
| **6380** | Onset | Tail Body | 4 | 11.6 | Female | African-American | 14.6 | T1D | 0.0 (2 days) |
| **6418** | Long-duration | Tail Body | 1 | 24.9 | Male | Caucasian | 26.4 | T1D | 11 |
| **6180** | Long-duration | Tail Body | 2 | 27 | Male | Caucasian | 25.9 | T1D | 11 |
| **6089** | Long-duration | Tail Body | 3 | 14.3 | Male | Caucasian | 26.0 | T1D | 8 |
| **6264** | Long-duration | Tail Head | 4 | 12 | Female | Caucasian | 22.0 | T1D | 9 |

| nPOD case ID | Auto-antibody status | C-peptide (ng/mL) | HbA1c (%) | Pancreas weight (g) | HLA |
|---|---|---|---|---|---|
| **6126** | Negative | 0.88 | N/A | 80.2 | A*29:02,33:01;DRB1*03:01,07:01;DQA1*02:01,05:01 DQB1*02:01,02:01 |
| **6134** | Negative | 3.59 | N/A | 82.4 | A*03:01,29:02; DRB1*07:01,10:01; DQA1*01:01,02:01; DQB1*02:01,05:01 |
| **6386** | Negative | 1.12 | 5.6 | 61.4 | A*02:01, 03:01;DRB1*04:04,13:01;DQA1*01:03,03:01;DQB1*03:02,06:03 |
| **6278** | Negative | 4.54 | 6.3 | 33.6 | A*23:01,68:02 DRB1*11:04,12:01 DQA1*03:01,05:01 DQB1*03:01,05:02 |
| **6362** | GADA+ | 0.38 | 10.0 | 53.3 | A*03:01,11:01;DRB1*01:03,03:01; DQA1*01:01,05:01;DQB1*02:01,05:01 |
| **6414** | GADA+ ZnT8+ mIAA+ | 0.16 | 14.0 | 98.5 | DRB1*03:01,09:01;DQA1*05:01,03:03;DQB1*02:01,02:02 |
| **6228** | GADA+ ZnT8+ IA-2A+ | 0.10 | 13.3 | N/A | A*23:01, 68:01;DRB1*03:01, 04:02;DQA1*03:01, 05:01;DQB1*02:01, 03:02 |
| **6380** | Negative | 0.22 | 13.5 | 34.3 | A*33:03,68:02; DRB1*03:01,13:02;DQA1*01:02,05:01; DQB1*02:01,06:04 |
| **6418** | GADA+ ZnT8+ IA-2A+ mIAA+ | < 0.02 | 7.5 | 28.6 | A*02/32 B*51/62 DR*04/11 DQ*07/08 |
| **6180** | GADA+ ZnT8+ IA-2A+ mIAA+ | < 0.05 | N/A | 36.7 | A*01:01,02:01; DRB1*01:01 ,03:01; DQA1*01:01 ,05:01; DQB1*02:01 , 05:01 |
| **6089** | mIAA+ | < 0.05 | 10.4 | 56.8 | A*01:01,02:01; DRB1*01:01,04:01; DQA1*01:01,03:01; DQB1*03:02,05:01 |
| **6264** | Negative | < 0.05 | 8.9 | 20.4 | A*23:01,32:01; DRB1*03:01 ,04:04;DQA1*03:01 ,05:01;DQB1*02:01,03:02 |

| nPOD case ID | Diabetes medications taken | Peak glucose during hospital stay (mg/dL) | Lipase (U/L) | Amylase (U/L) | Hospitalization stay days | Cause of death |
|---|---|---|---|---|---|---|
| **6126** | None | 272 | 546 | 164 | 4.88 | Head trauma |
| **6134** | None | N/A | 40 | 175 | 2.02 | Anoxia |
| **6386** | None | 198 | N/A | N/A | 2.34 | Head trauma |
| **6278** | None | 395 | 11 | 100 | 1.84 | Anoxia |
| **6362** | Insulin IV (drip) on admission | 435 | N/A | N/A | 7.76 | Head trauma |
| **6414** | NovoLog Lantus | 690 | N/A | N/A | 4.63 | Anoxia |
| **6228** | None | 664 | 45 | 33 | 10.04 | Anoxia |
| **6380** | None | 1661 | N/A | N/A | 4.02 | Diabetes ketoacidosis, Cerebral edema |
| **6418** | Insulin (injections and pump) | 400 | N/A | N/A | 5.25 | Anoxia |
| **6180** | NovoLog (pump) | 363 | 14 | 26 | 5.53 | Head trauma |
| **6089** | Humalog Lantus | 750 | 3000 | 736 | 2.79 | Anoxia |
| **6264** | Humalog NovoLog Lantus | 641 | N/A | N/A | 2.13 | Diabetic ketoacidosis |

**Table S2. Antibody Validation. Related to STAR Methods**

| PANCREAS | | |
|---|---|---|
| **Short name** | **Target protein** | **Evidence for antibody validation** |
| INS | Insulin | This antibody is validated for IHC on paraffin-embedded sections by Cell Signaling Technologies and has been used in many (>20) studies.<br>***Our observations - Pancreas*:** Detected in islets only, in the same cells as proinsulin, amylin and Nkx6.1. No colocalization with other pancreatic hormones.<br>***Other tissues:*** Not detected |
| PIN | Proinsulin | This antibody reacts with the site of connection of C-peptide and C-end of B-chain of proinsulin molecule. It is validated for IHC by Abcam and has been used in several studies.<br>***Our observations - Pancreas*:** Detected in islets only, in the same cells as insulin, amylin and Nkx6.1, but with a slightly different subcellular distribution as compared to insulin. No colocalization with other pancreatic hormones.<br>***Other tissues:*** Not detected |
| GCG | Glucagon | This antibody is validated for IHC on paraffin-embedded sections by Cell Signaling Technologies and has been used in several studies.<br>***Our observations - Pancreas:*** Detected in islets only, no colocalization with other pancreatic hormones.<br>***Other tissues:*** Detected in duodenum enteroendocrine cells (proglucagon) |
| SST | Somatostatin | This antibody is validated for IHC by Dako and has been used in many studies.<br>***Our observations - Pancreas:*** Detected in islets only, no colocalization with other pancreatic hormones.<br>***Other tissues:*** Detected in duodenum and colonic enteroendocrine cells. |
| PPY | Pancreatic polypeptide | This antibody is validated for IHC on paraffin-embedded sections by R&D Systems.<br>***Our observations - Pancreas:*** Detected in islets only, no colocalization with other pancreatic hormones.<br>***Other tissues:*** Not detected |
| NKX6-1 | Nkx6.1 | This antibody is validated for IHC on paraffin-embedded sections by Cell Signaling Technologies.<br>***Our observations - Pancreas:*** Detected in islets only, in cells positive for (pro-)insulin. Nuclear expression pattern.<br>***Other tissues:*** Not detected. |
| PDX1 | Goat IgG (goat anti-Pdx1) | This antibody is validated for IHC on paraffin-embedded sections by R&D Systems and has been used in several studies.<br>***Our observations - Pancreas:*** Detected in islets, in cells positive for (pro-)insulin and somatostatin. Also expressed in pancreatic ductal cells. Signal stronger in nucleus than in cytoplasm.<br>***Other tissues:*** Positive cells observed in the duodenum. Also observed in enteroendocrine cells in the colon (together with somatostatin). Background signal observed in several tissues. |
| IAPP | Amylin | This antibody is validated for IHC on paraffin-embedded sections by Sigma and additionally validated for the Human Protein Atlas project.<br>***Our observations - Pancreas:*** Detected in islets only, in the same cells as (pro-)insulin. No colocalization with pancreatic hormones.<br>***Other tissues:*** Background signal detected in a few tissues (skeletal muscle, duodenum, placenta). |
| PCSK2 | Prohormone convertase 2 | This antibody is validated for IHC by Merck.<br>***Our observations - Pancreas:*** Detected in islets only. Signal highest in α cells.<br>***Other tissues:*** Positive cells observed in duodenum. Background signal observed in several tissues. |
| SYP | Synaptophysin | This antibody is validated for IHC on paraffin-embedded sections by Abcam and has been used in many studies.<br>***Our observations - Pancreas:*** Detected in islets, overlap with pancreatic hormones and with CD99. Also detected in pancreatic neuroendocrine carcinoma.<br>***Other tissues:*** High levels detected in cerebral cortex. |

| | | |
|---|---|---|
| CD99 | CD99 | This antibody is validated for IHC on paraffin-embedded sections by BioLegend.<br>***Our observations - Pancreas:*** Very high signal in islets, overlaps with synaptophysin. Detected at much lower levels in exocrine cells and some immune cells. Also detected in pancreatic neuroendocrine carcinoma.<br>***Other tissues:*** Detected in a wide range of tissues. High levels observed in spleen. |
| SLC2A1 | Glucose transporter 1 | This antibody is validated for IHC on paraffin-embedded sections by Abcam and has been used in many studies.<br>***Our observations - Pancreas:*** Highest signal observed in islet cells.<br>***Other tissues:*** High signal in endothelial cells of the cerebral cortex and in the microvillus and basal membranes of the placenta. High signal in several cancer samples (urothelial, breast and ovarian carcinoma; lung, uterus and colorectal mucinous adenocarcinoma; melanoma). |
| PTPRN | Receptor-type tyrosine-protein phosphatase-like N | This antibody is validated for IHC on paraffin-embedded sections by Sigma and additionally validated for the Human Protein Atlas project.<br>***Our observations - Pancreas:*** Detected in all islet cells.<br>***Other tissues:*** Detected in the enteric neuronal cells in the muscular layers of the duodenum (colocalized with Synaptophysin). |
| AMY2A | Pancreatic amylase | This antibody is validated for IHC on paraffin-embedded sections by Abcam and has been used in several studies.<br>***Our observations - Pancreas:*** Detected only in exocrine tissue. Staining pattern consistent with acinar cells. No overlap with islet and ductal (KRT19) markers.<br>***Other tissues:*** Not detected. |
| KRT19 | Cytokeratin 19 | This antibody is validated for IHC on paraffin-embedded sections by Cell Signaling Technologies.<br>***Our observations - Pancreas:*** Detected only in exocrine tissue. Staining pattern consistent with ductal cells. Detected in the same cells as Sox9 in a parallel experiment.<br>***Other tissues:*** Detected in colon and uterus epithelial cells, and in kidney tubules |
| CD44 | CD44 | This clone is validated for IHC on paraffin-embedded sections by BD Biosciences and has been used in many studies.<br>***Our observations - Pancreas:*** Detected in subsets of exocrine cells and in some immune cells.<br>***Other tissues:*** Detected in large subsets of immune cells and in a wide range of tissues. |

| **IMMUNE** | | |
|---|---|---|
| **Short name** | **Target protein** | **Evidence for antibody validation** |
| CD45 | CD45 | This antibody is validated for IHC on paraffin-embedded sections by eBioscience and has been used in several studies.<br>***Our observations:*** Staining pattern consistent with immune cells in lymphoid and other tissues. |
| CD45RA | CD45RA | This clone is validated for CyTOF and IHC by Biolegend, Fluidigm and other companies and was internally validated by suspension mass cytometry. It has been used in many studies.<br>***Our observations:*** In the pancreas, detected in B cells and in a subset of T cells. In lymphoid tissues, detected in B cells and in subsets of other immune cells. |
| CD3e | CD3ε | This antibody is validated for IHC on paraffin-embedded sections by Cell Signaling Technologies.<br>***Our observations:*** detected in a subset of CD45-positive cells. Colocalized with either CD4 or CD8 in the pancreas and in lymphoid tissues. Staining pattern in lymphoid tissues consistent with T cells. |
| CD4 | CD4 | This antibody is validated for IHC on paraffin-embedded sections by R&D Systems and has been used in several studies.<br>***Our observations:*** Detected in a subset of $CD45^+$ $CD3e^+$ cells in the pancreas and in lymphoid tissues. No overlap with CD8a observed. |
| CD8a | CD8a | This clone is validated for IHC on paraffin-embedded sections by eBioscience and other companies, and has been used in many studies.<br>***Our observations:*** Detected in a subset of $CD45^+$ $CD3e^+$ cells in the pancreas and in lymphoid tissues. No overlap with CD4 observed. |
| CD20 | CD20 | This clone is validated for IHC on paraffin-embedded sections by eBioscience and other companies, and has been used in many studies.<br>***Our observations:*** Detected in a subset of $CD45^+$ cells in the pancreas and lymphoid tissues. Staining pattern in lymphoid tissues consistent with B cells. |

| | | |
|---|---|---|
| CD68 | CD68 | This clone is validated for IHC on paraffin-embedded sections by eBioscience and other companies, and has been used in many studies.<br>***Our observations:*** Expression pattern consistent with macrophages/monocytes in internal cross-validations with anti-CD163 and anti-CD16 antibodies. Also detected in fibroblasts, which has been reported for this clone. |
| MPO | Myeloperoxidase | This antibody is validated for IHC on paraffin-embedded sections by Dako and has been used in many studies.<br>***Our observations:*** Staining pattern consistent with neutrophils in the spleen. |
| FOXP3 | Forkhead box P3 | This clone is validated for IHC on paraffin-embedded sections by eBioscience and other companies, and was internally validated by suspension mass cytometry. It has been used in many studies.<br>***Our observations:*** Nuclear signal observed in a small subset of $CD4^+$ cells. |
| CD38 | CD38 | This antibody is validated for IHC on paraffin-embedded sections by Abcam and was internally validated by suspension mass cytometry. It has been used in several studies.<br>***Our observations:*** Expressed in a wide range of cells and tissues. |

| **MISC** | | |
|---|---|---|
| **Short name** | **Target protein** | **Evidence for antibody validation** |
| CDH | E-/P-cadherin | This antibody is validated for IHC by BD Biosciences and has been used in many studies.<br>***Our observations:*** Detected in both exocrine and islet cells in the pancreas. Staining pattern consistent with epithelial cells in all tissues analyzed. |
| CD31 | CD31 | This antibody is validated for IHC on paraffin-embedded sections by Novus and has been used in many studies.<br>***Our observations:*** Pattern consistent with endothelial cells in all tissues analyzed. SMA staining often detected around large $CD31^+$ blood vessels. |
| SMA | Smooth muscle actin | This antibody is validated for IHC on paraffin-embedded sections by Abcam and has been used in several studies.<br>***Our observations:*** Detected in smooth muscle. Signal also commonly observed around large blood vessels. |
| KI-67 | Ki-67 | This antibody is validated for bioimaging by BD Biosciences and has been used in many studies.<br>***Our observations:*** Nuclear expression pattern, consistent with proliferating cells in all tissues analyzed. Often colocalized with pRB1. |
| pH3 | Phospho-histone H3 | This clone is validated for IHC on paraffin-embedded sections and CyTOF by Biolegend, Fluidigm and other companies. It has been used in many studies.<br>***Our observations:*** Nuclear staining pattern. Sometimes colocalized with Ki-67. Unspecific signal in skeletal muscle (sarcomeres) but the signal is clearly distinct from the nuclear signal observed in dividing cells. |
| pRB1 | Phospho-retinoblastoma | This antibody is validated for IHC on paraffin-embedded sections by Cell Signaling Technologies and has been used in many studies.<br>***Our observations:*** Staining pattern consistent with cycling cells. Often colocalizes with Ki-67. |
| cPARP1 | Cleaved caspase 3 + poly (ADP-ribose) polymerase | These anti-caspase 3 antibody is validated for IHC on paraffin-embedded sections by BD biosciences and has been used in many studies. Both antibodies have been validated internally for suspension and imaging mass cytometry.<br>***Our observations:*** Very few positive cells observed in all analyzed tissues. |
| CA9 | Carbonic anhydrase IX | This antibody is validated for IHC on paraffin-embedded sections by R&D Systems and has been used in several studies.<br>***Our observations:*** Detected in duodenum crypt cells and in several cancer samples (e.g. clear renal cells and urothelial cell carcinoma) |
| H3 | Histone H3 | This antibody is validated for IHC on paraffin-embedded sections by Cell Signaling Technologies and has been used in many studies.<br>***Our observations:*** Detected only in nuclei, in all tissues analyzed. |